Thin-Walled Structures 191 (2023) 110996

Contents lists available at ScienceDirect

Thin-Walled Structures

journal homepage: www.elsevier.com/locate/tws

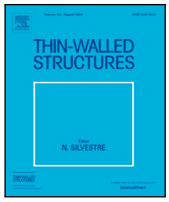

Full length article

Experimental behaviour of large-size beam-to-column steel joints for the DUNE Neutrino Experiment

L. Simões da Silva [a,*], Hélder Craveiro [a], Jorge Conde [b], Rui Simões [a], Claúdio Martins [a], Andrea Catinaccio [c], Dimitar Mladenov [c], João Batista Lopes [c], Diego Alvarez Feito [c], Christophe Bault [c]

[a] University of Coimbra, ISISE, ARISE, Department of Civil Engineering, Portugal
[b] Universidad Politécnica de Madrid, Departamento de Física y Estructuras de Edificación, Spain
[c] CERN, Switzerland

ARTICLE INFO

Keywords:
Large joints
Experimental
Beam-to-column steel joint
Moment–rotation
Eurocode 3

ABSTRACT

This paper reports on an experimental investigation on a very large, bolted beam-to-column steel joint that will be extensively used in a new experimental facility for the study of neutrinos (DUNE experiment), hosted by the U.S. Department of Energy's Fermilab. The dimensions of the members (HL 1100 in S460 steel) are uncommonly large at an experimental level and, consequently, the gathered experimental data is of utmost importance for the validation of the component method for large-size steel joints. The steel joint is subjected to static monotonic loading. Relevant instrumentation was used to monitor and assess the moment–rotation characteristics, experimental stiffness, and moment resistance. The experimental results are presented and analysed. Comparisons with design predictions according to EN 1993-1-8 and state-of-the-art FEA, show an excellent agreement, validating the application of the component method for very large joints.

1. Introduction

A mega scientific experimental project for the study of neutrinos and proton decay, the Deep Underground Neutrino Experiment (DUNE), is being developed by the global physics community. This new experiment requires a specific laboratory facility, the Long-Baseline Neutrino Facility (LBNF), hosted at Fermilab in Batavia, Illinois, USA. The world's highest-intensity neutrino beam will be installed in the LBNF facility, which will also have the necessary infrastructure to support the cryogenic far detectors installed underground at the Sanford Underground Research Facility [1]. The cryogenic tank installed in these new facilities is supported by a large carbon steel outer structure made from large hot-rolled steel profiles (HL1100M) fabricated with high-strength steel (S460ML), schematically shown in Fig. 1.

The outer steel structure of the cryogenic tank (warm vessel), designed by CERN, has the following dimensions: 66 m × 19 m × 18 m. It comprises large, bolted beam-to-column joints using massive preloaded M48 class 10.9 bolts.

Predicting the mechanical behaviour of bolted beam-to-column steel joints can be a complex task [2], and several approaches may be used to achieve it, such as empirical models, analytical models such as component models (CM), mechanical models, finite element models (FEM) and experimental testing [3,4]. Since the 1970s, the key components that control the behaviour of bolted steel joints such as the T-Stub [5–7], the column web panel in shear [8,9], and the load-introduction components [9,10] were identified and studied, leading to design models that can predict the moment resistance of a bolted joint as well as its deformability. These developments were incorporated in design codes [11,12] and allow: (i) to take advantage of plastic redistribution in the case of ductile joints, with significant gains in moment resistance when compared to traditional empirical design procedures based on elastic distributions of forces between the bolt rows; (ii) correctly identify the failure mode of such joints.

These developments were naturally supported by extensive experimental test campaigns, collected in various databases [13–16], exceeding 650 full-scale static monotonic and cyclic experimental tests on steel and composite joints. However, despite this large number of tests, most of the tests on beam-to-column steel joints were conducted considering hot-rolled beams with a total depth of up to 600 mm. Even enlarging the scope to beam splice joints, the number of tests on beam splices between large-size steel members is scarce [17–22].

It is obvious why the number of reported tests on the large size and high-capacity beam-to-column (bolted and welded) joints is quite limited due to the inherent difficulties in performing such tests (time, laboratory facilities, equipment constraints, etc.) [23], hence limiting

* Correspondence to: Civil Engineering Department, University of Coimbra, 3030-799 Coimbra, Portugal.
E-mail address: luisss@dec.uc.pt (L. Simões da Silva).

https://doi.org/10.1016/j.tws.2023.110996
Received 10 February 2023; Received in revised form 6 June 2023; Accepted 1 July 2023
Available online 7 August 2023

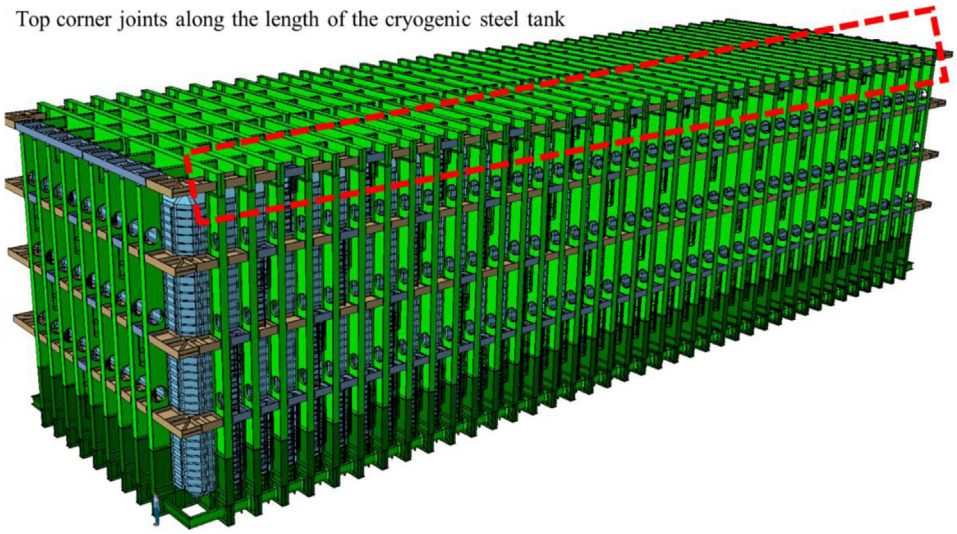

Fig. 1. Schematic 3D representation of the steel structure of the cryogenic tank defining the position of the tested beam-to-column joint.

the possibility of assessing the suitability and accuracy of the currently available design codes for large steel joints. This raised the question of whether the developed design rules and the component method would still hold for large steel profiles, namely the possibility to consider plastic distributions of bolt forces with many bolt rows and deep profiles. This led those responsible for the DUNE experiment to request full-scale experimental testing of all the different joints present in the steel structure of the cryogenic tank. Hence, this paper reports on the experimental results of one full-scale test on a large-size bolted end-plate beam-to-column joint connecting two hot-rolled HL1100M steel profiles fabricated in high-strength steel (S460ML). The experimental programme, behaviour of the steel joints, experimental moment–rotation curves, stiffness, and failure modes are discussed. Moreover, as the use of the finite element method is crucial to get a deeper understanding of the behaviour of large size and high-capacity steel joints [24], the experimental results are then compared with high-quality FEA models. Finally, the component method is applied, and its validity is assessed in the scope of the EN 1993-1-8 [11] design prescriptions.

2. Experimental programme

2.1. General description

The experimental programme comprises the execution of a full-scale experimental test on one exceptionally large beam-to-column steel joint. Hereby, this bolted beam-to-column steel joint is referred to as C2 test specimen. The main objective was to assess the behaviour of the joint under static monotonic loading, aiming to attain a specific performance target representative of serviceability design forces increased by 25%. However, the test was carried out well beyond this level, up to the ultimate load. Also, in the scope of this investigation, the detailed material characterization was undertaken, for both profiles and bolts.

The C2 test specimen, shown in Fig. 2, was a bolted beam-to-column steel joint, connecting two HL1100M steel profiles fabricated in S460ML, with the following nominal cross-section geometry: depth $h = 1108\,\text{mm}$, width $b = 402\,\text{mm}$, flange thickness $t_f = 40\,\text{mm}$, web thickness $t_w = 22\,\text{mm}$, and root radius $r = 30\,\text{mm}$, see Fig. 3(a). The real geometrical properties were measured and are in line with the variability of dimensional properties assumed in Annex E of prEN 1993-1-1 [25]; thus, for the sake of simplicity, nominal properties are used throughout this paper. The joint was assembled with preloaded HR-M48-10.9 bolts (hereinafter referred simply as 'HR' bolts), in 52 mm clearance holes. Eight bolt-rows with two bolts per bolt-row (total of 16 bolts) were considered and the spacing between bolt-rows was $p_1 = 120\,\text{mm}$ with an end distance $e_1 = 154\,\text{mm}$. The edge distance was $e_2 = 113\,\text{mm}$ and the spacing between bolts of the same row was $p_2 = 176\,\text{mm}$. Relevant joint details are shown in Fig. 3(a). The attachment to the reaction wall is solved with an auxiliary joint (hereinafter referred to as joint CA), defined in Fig. 3(b). The test setup is rotated 90° concerning the real structural configuration; for this reason, the column is presented as horizontal, whereas the beam is vertical. This member layout is consistently kept in all figures throughout the manuscript for clarity.

2.2. Test layout and instrumentation

In the test, a reinforced concrete reaction wall was used to fix the specimen as well as the high-capacity hydraulic jack. Connection CA was designed and manufactured to attach the test specimen to the reaction wall of the laboratory. To achieve the desired levels of versatility, ease of assembly and disassembly the fixation system comprised two large L-shape stiffened plates bolted to the web of the specimen using HV-M48-10.9 bolts (see Figs. 2 and 3); these bolts are referred hereby as 'HV'. The large, stiffened L-shape plates were fixed to the reaction wall using twenty ϕ36 Dywidag bars. At the other end of the specimen, a roller support was positioned at the bottom-left corner, preventing vertical displacements at the specimen's end (Fig. 4).

The loading was applied by a 6 MN high-capacity hydraulic jack, horizontally positioned, and fixed to the reaction wall. The hydraulic jack was controlled by a servo hydraulic control unit. A high-capacity load cell (6 MN) was attached to a thick plate, simply in contact with the beam face (no fasteners), that defined the load application area (402 mm × 400 mm).

To prevent unwanted stability problems the test specimen was laterally restrained at some locations by steel beams (light blue pieces in Fig. 4(b)), supported by the steel reaction frame.

Fig. 5(a) shows the free-body diagram for the joint test and defines the notation for the key points used throughout this paper. The system is statically indeterminate. The load F_E is applied at point E, producing an internal positive bending moment M_F at point F, resulting in tensile stresses at the joint inner corner. The distribution of this bending moment on the column is dependent on the boundary conditions. Whereas point B is clearly a simple support, point A presents a degree of rotational stiffness, comprised within two extreme situations: fully pinned, Fig. 5(b) and, fully fixed, Fig. 5(c). The structure is analysed for both situations under a load $F_E = 2284.4$ kN, assuming a rigid connection with infinite stiffness at point F. The results, shown in Table 1, indicate

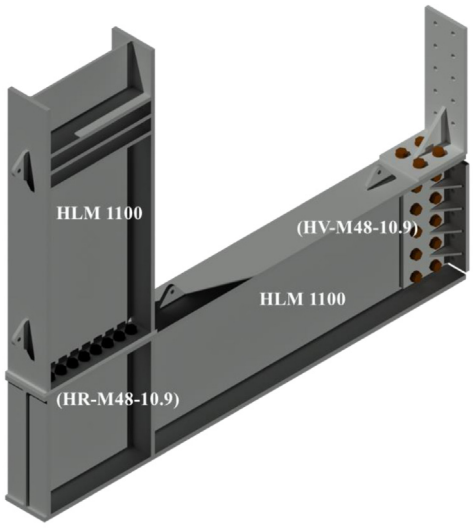

(a)

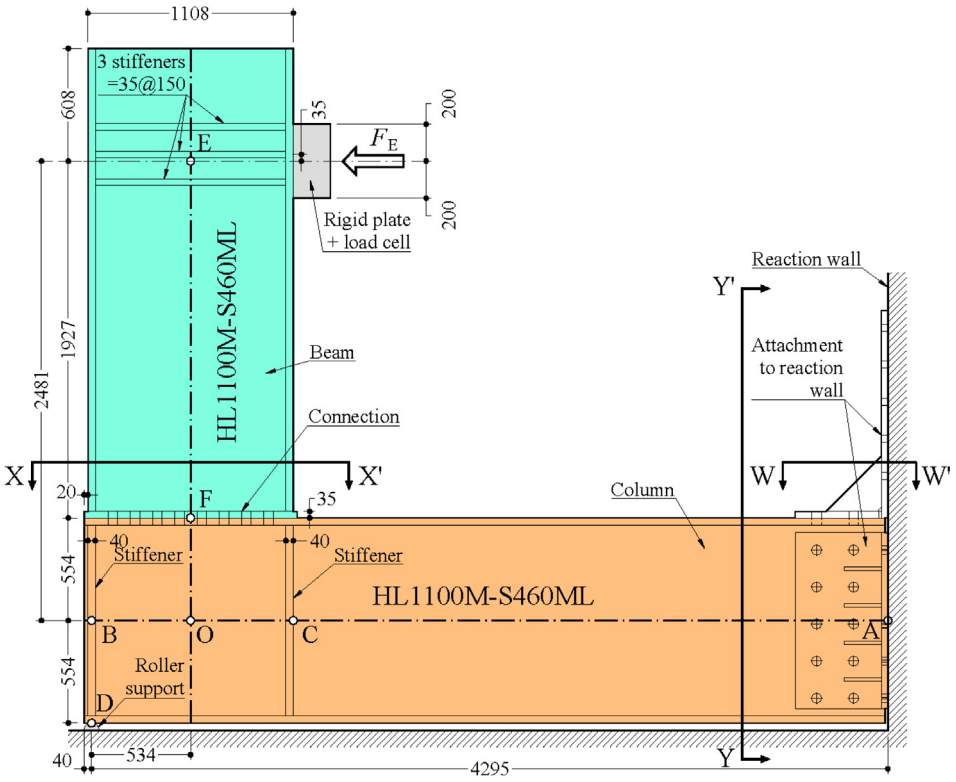

(b)

Fig. 2. Geometry of test setup: (a) 3D view; (b) elevation.

a reduction of about 311.3 kN in the reaction N when the rotational stiffness of point A reaches zero, that is, −19.1% of the value obtained with a fixed support, whereas the internal moment M_C changes only by 8.5%. This variation is small, showing a relatively low sensitivity of the joint behaviour to the rotational stiffness of the connection at point A. The simply supported option is statically determinate, whereas the fixed option is statically indeterminate. Interestingly, the simply supported option displays higher displacements at point E than the fixed option, for the same applied load.

The instrumentation is defined and detailed in Fig. 6 for the LVDTs (Linear Variable Differential Transformers). The positioning of the instrumentation was defined aiming to accurately estimate the experimental moment–rotation curve of the tested specimens. The position of strain gauges and some of the obtained results are presented in Supplementary Material.

2.3. Loading protocol

The loading protocol comprised the 5 steps detailed in Table 2 indicating the target forces to be achieved. The load/unload steps were also considered to eliminate initially existing gaps in the experimental system and to allow for a more accurate assessment of the initial stiffness of the joint. A load target was initially defined, based on the maximum design internal forces of the real joint, $M_{Ed,max} = 2933.8$ kN·m (bending moment) and $V_{Ed,max} = 1442.8$ kN (shear force), measured at

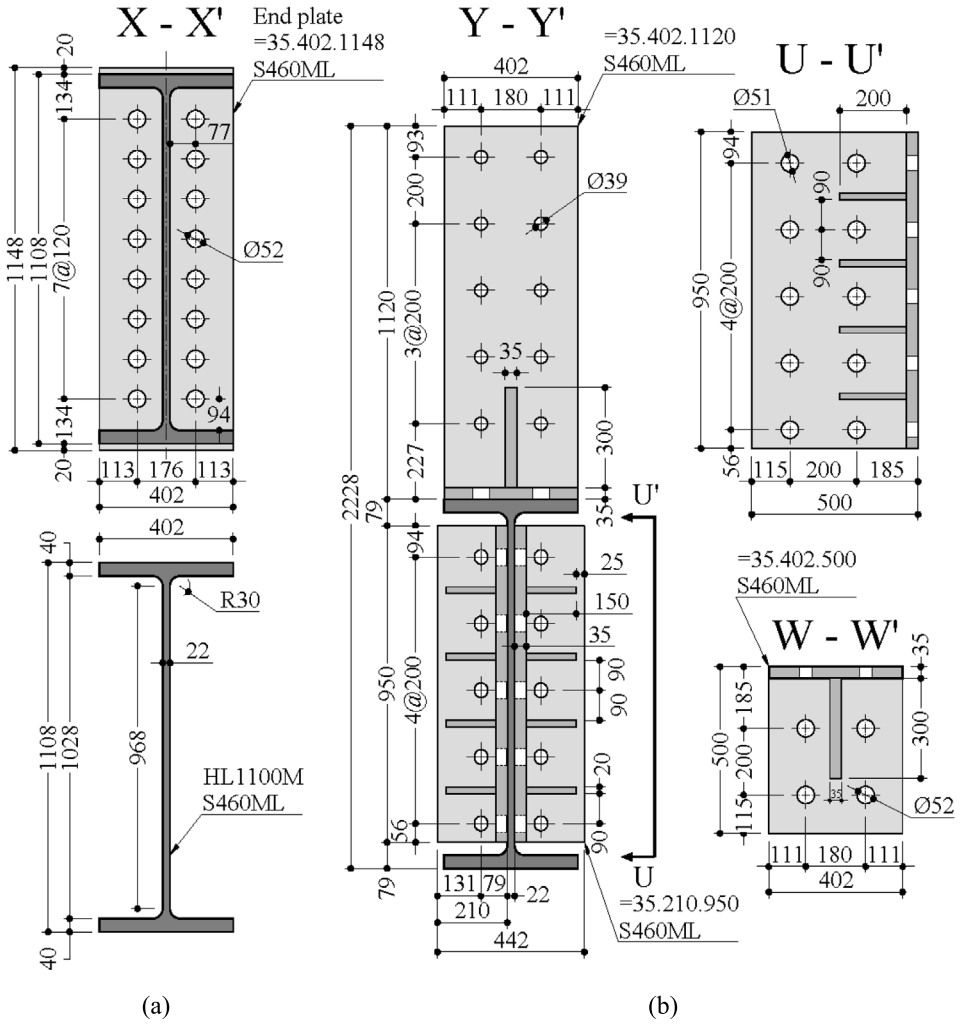

Fig. 3. Details of specimen: (a) beam–column connection; (b) attachment to reaction wall.

Table 1
Internal forces and reactions at key points assuming different boundary conditions.

		(1) Fixed support at A	(2) Simple support at A	(3) (2)–(1)	(4) (3)/(1)
M_F	kN·m		4402.0	0	0
$M_{O,beam}$	kN·m		5667.6	0	0
N	kN	1629.4	1318.1	−311.3	−19.1%
M_A	kN·m	1338.7	0	−1338.7	−100%
M_C	kN·m	3927.4	4259.9	332.5	8.5%

the column face (point F in Fig. 5) and provided by the final user of the joint. In Table 2, the indicated forces correspond to the most severe design situations, increased by 25%.

After attaining the target contractual forces defined in step_1 to step_3, the specimen was loaded up to a maximum load of 3158.9 kN, attained at the displacement limit of the hydraulic jack, including intermediate unloading (step_4). The load was applied under displacement control, using an external LVDT to control the displacement rate. A quasi-static, displacement control test was executed, adopting a displacement rate of approximately 0.01 mm/s, up to the established target forces or until failure.

2.4. Mechanical properties of steel

To fully characterize the mechanical properties of the steel of hot-rolled steel profiles and bolts, tensile coupon tests for both elements were fabricated and tested according to the ISO 6892-1 standard [26]. Tensile coupon specimens were extracted from the HL1100M steel profiles (from both flange and web, parallel and perpendicular to the rolling direction), steel plate used for stiffeners, end plates, and M48 bolts. A total of 15 flat coupon specimens and 6 cylindrical ones were machined. The flat specimens had a total length of 300 mm, a gauge length of 125 mm, a thickness of 25 mm and a width of 20 mm, whereas the cylindrical ones had a total length of 200 mm, a gauge length of 100 mm and a diameter of 20 mm. An Instron extensometer was used in the experimental tests. From the experimental tests, it was possible to determine the yield strength, ultimate strength, and total elongation after fracture as well as the stress–strain relationship. The obtained results are extremely important not only for characterization purposes but also to be used as input in advanced calculation models using FEM, aiming to obtain a good agreement between experimental and numerical results. The obtained experimental results are presented in Annex A (Table A.1, Table A.2, Table A.3 and Table A.4) for the coupon specimens extracted from the web, flanges, end plate and bolts,

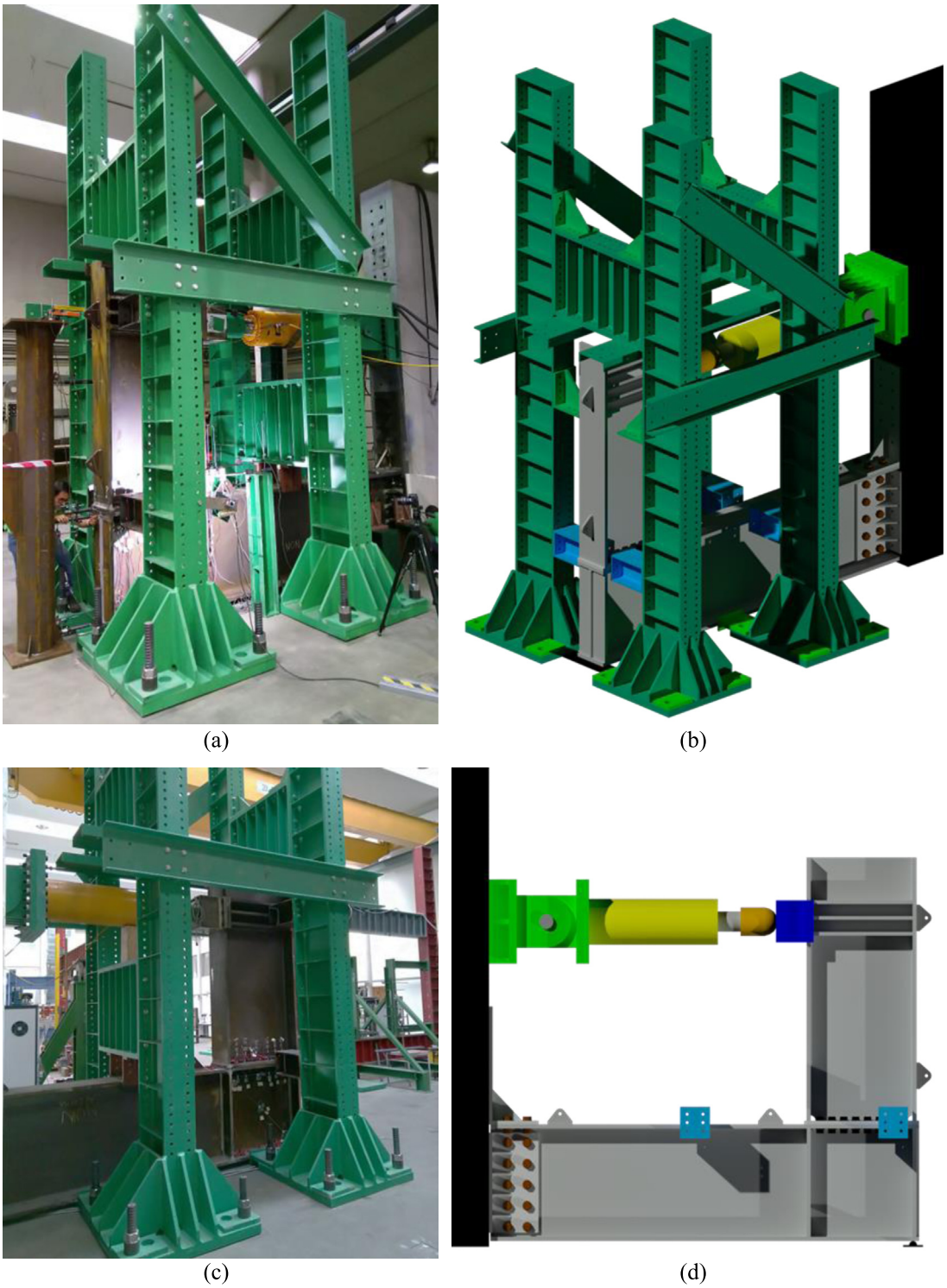

Fig. 4. Schematic representation of the test setup: (a) global view; (b) detail of the fixation system and loading system; (c) and (d) different views of the test setup.

Table 2
Target forces for the test.

Steps	Target	Notes	$F_E = V$ [kN]	M_F [kN·m]
Step_1	20% × 1.25 × $V_{Ed,max}$	Load/Unload	360.7	695.1
Step_2	1.25 × $V_{Ed,max}$	Load	1803.5	3475.3
Step_3	1.25 × $M_{Ed,max}$	Load/Unload	1903.1	3667.3
Step_4	120% × 1.25 × $M_{Ed,max}$	Load/unload	2284.4	4402.0
Step_5	Repeat Step_4 + specimen tested up to displacement limit of hydraulic jack			

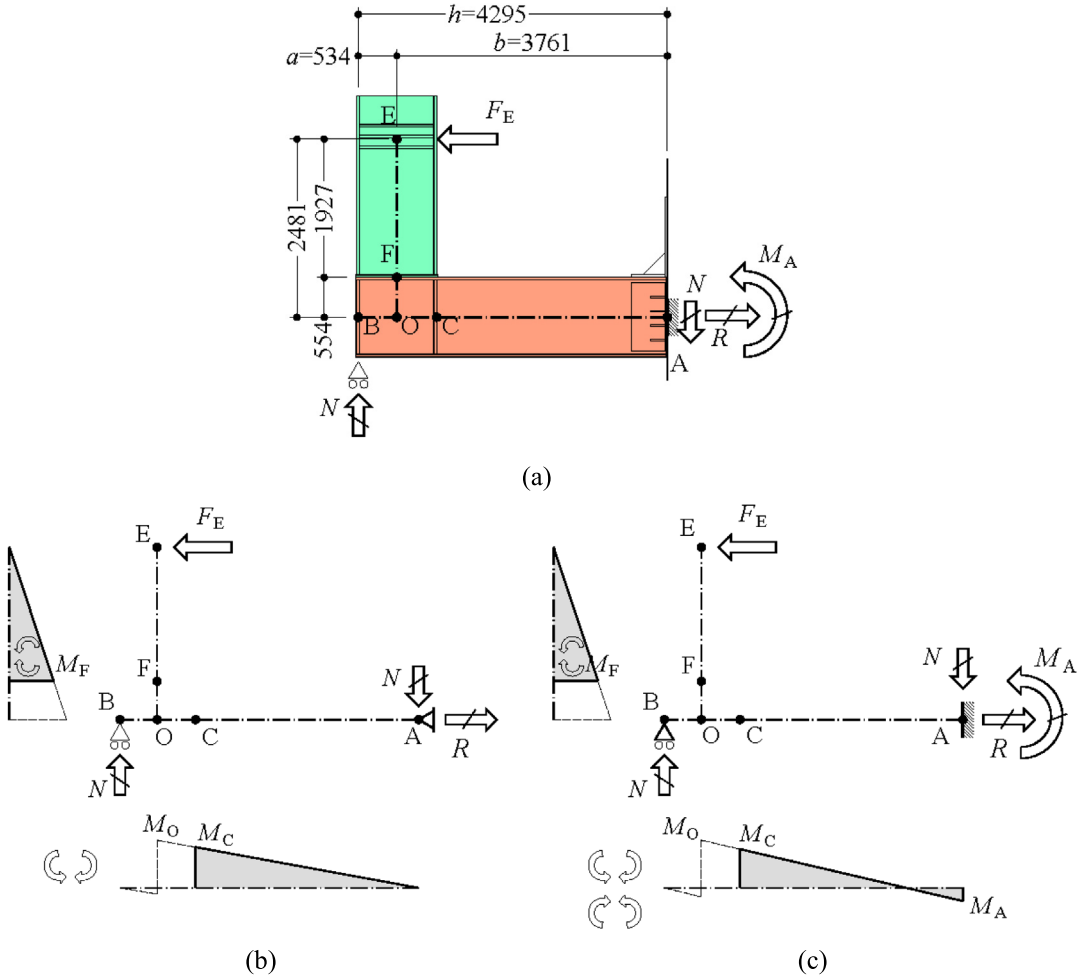

Fig. 5. Statics of the tests: (a) geometrical definition; (b) simple support; (c) fixed support.

Table 3
Summary of average values from coupon tests.

Sample	E [GPa]	f_y [N/mm^2]	f_u [N/mm^2]	ε_u [%]
Web, parallel to rolling direction	199.9	464.7	594.0	10.49
Web, perpendicular to rolling direction	210.6	470.7	613.7	9.77
Flange, parallel to rolling direction	195.4	496.7	605.0	10.91
Flange, perpendicular to rolling direction	194.5	464.0	589.3	11.83
End plate, parallel to rolling direction	193.7	516.7	590.3	8.18
HR-M48-10.9	209.4	921.0	1035.7	5.35
HV-M48-10.9	199.8	1060.0	1149.7	3.61

respectively. For the coupon specimens extracted from the bolts the total length was 200 mm, the gauge length was 100 mm and the diameter was 20 mm. For the coupons extracted from the steel profiles the total length was 300 mm, the gauge length was 125 mm, the thickness was 25 mm and the width was 20 mm. For the coupons extracted from the end-plate the total length was 300 mm, the gauge length was 125 mm, the thickness was 25 mm and the width 20 mm. The average yield strength (f_y) is taken as the stress at the 0.2% residual stress point ($R_{p,0.2\%}$) defined in [26], whereas the tensile strength (f_u) is taken as the tensile stress (R_m), defined in the same standard. The relevant as-measured values, obtained as the average of the coupon tests, are presented in Table 3. The complete stress–strain diagrams are shown in Fig. 7 (steel profiles), Fig. 8 (bolts) and Fig. 9 (end plates).

The results obtained for the S460ML steel satisfy the minimum values defined in EN 10025-4 [27] both in terms of yield strength, tensile strength, and minimum elongation after fracture, namely, for a plate thickness between 16 and 40 mm the minimum yield strength shall be 440 MPa, the minimum tensile strength shall be higher than 540 and lower than 720 MPa and the minimum elongation after fraction shall be 17%. For the HV bolts the obtained results satisfy the minimum values defined in ISO 898-1 [28]. For the HR bolts, however, the determined mechanical properties (1035.7 MPa and 921 MPa) are slightly below the minimum values defined in the standard, namely, the minimum tensile strength defined for class 10.9 shall be 1040 MPa, the minimum stress at 0.2% non-proportional elongation shall be 940 MPa, and the minimum percentage elongation after fracture shall be 9%.

All experimental data gathered were subsequently used in the FEM and CM models.

2.5. Global experimental results

During the test, the maximum recorded shear force applied to the joint was $F_E = 3158.9$ kN ($2.19 \times V_{Ed,max}$), and the corresponding bending moment in the joint (point F in Fig. 5) was $M_F = 6166.3$ kN·m ($2.1 \times M_{Ed,max}$), whereas at the centreline intersection of the two connected elements (point O in Fig. 5) it reached $M_O = 7837.2$ kN·m.

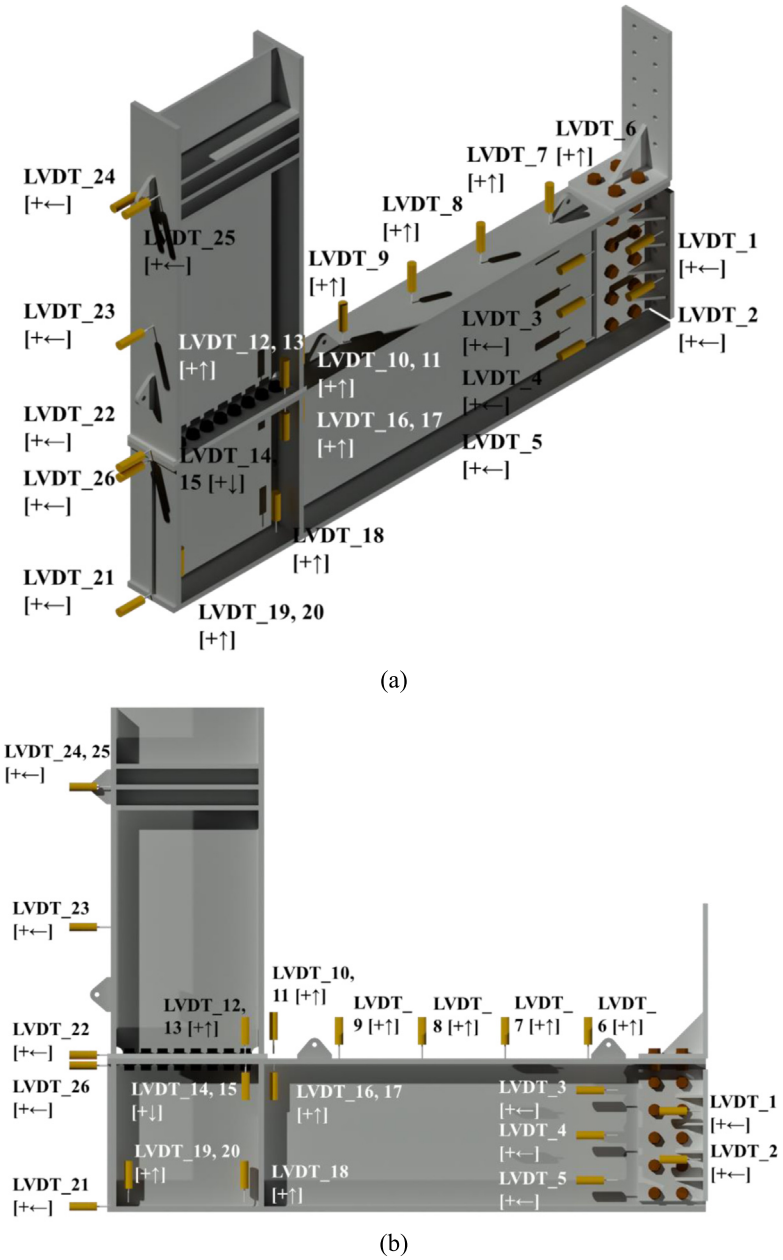

Fig. 6. LVDTs on C2 test specimen. (a) 3D view. (b) Elevation view.

From the data collected from the experimental test, it was also possible to determine the real horizontal displacement of the specimen, excluding the deformability of the joint connecting the specimen to the reaction wall (joint CA) and the elongation of the Dywidag bars used to fix the specimen to the reaction wall. In Fig. 10 the force–displacement curve of the specimen, excluding both the deformation of joint CA and the elongation of the Dywidag bar is presented for all steps (according to the steps defined in Table 2). As previously detailed, the initial loading steps were also considered to eliminate existing gaps and allow some adjustments in such a large experimental system (Fig. 10(a) and Fig. 10(b)). After the initial load/unload steps, the joint was loaded until failure. Focusing on this last step the previous data was neglected and a new plot was generated, considering a translation of the data to the origin of the graph (Fig. 10(c)).

For the moment–rotation curve, the horizontal rigid body motion is not relevant, as it does not affect the rotation. The maximum shear force and bending moment occurred for a horizontal deflection of approximately 139.2 mm, measured at the load application point and excluding the deformability of joint CA and the elongation of the Dywidag bars. The moment–rotation pairs corresponding to each load step in the test were determined as:

$$M_{\mathrm{F}} = F_{\mathrm{E}}\, d_{\mathrm{EF}}, \tag{1}$$

$$\phi = \phi_{endplate} - \phi_{column}, \tag{2}$$

$$\phi_{endplate} \approx \tan^{-1}\left(\frac{\frac{LVDT_{10}+LVDT_{11}}{2} - \frac{LVDT_{19}+LVDT_{20}}{2}}{d_{10-19}}\right), \tag{3}$$

$$\phi_{column} \approx \tan^{-1}\left(\frac{LVDT_{26} - LVDT_{21}}{d_{26-21}}\right), \tag{4}$$

where $d_{\mathrm{EF}} = 1.927$ m is the vertical distance between points E and F (see Fig. 5), ϕ is the joint rotation, $LVDT_n$ is the displacement measured by LVDT number n, and d_{n-m} is the distance between parallel LVDTs n and m, measured orthogonal to their lines of displacement.

The force–displacement and moment–rotation curves exhibit the following stages:

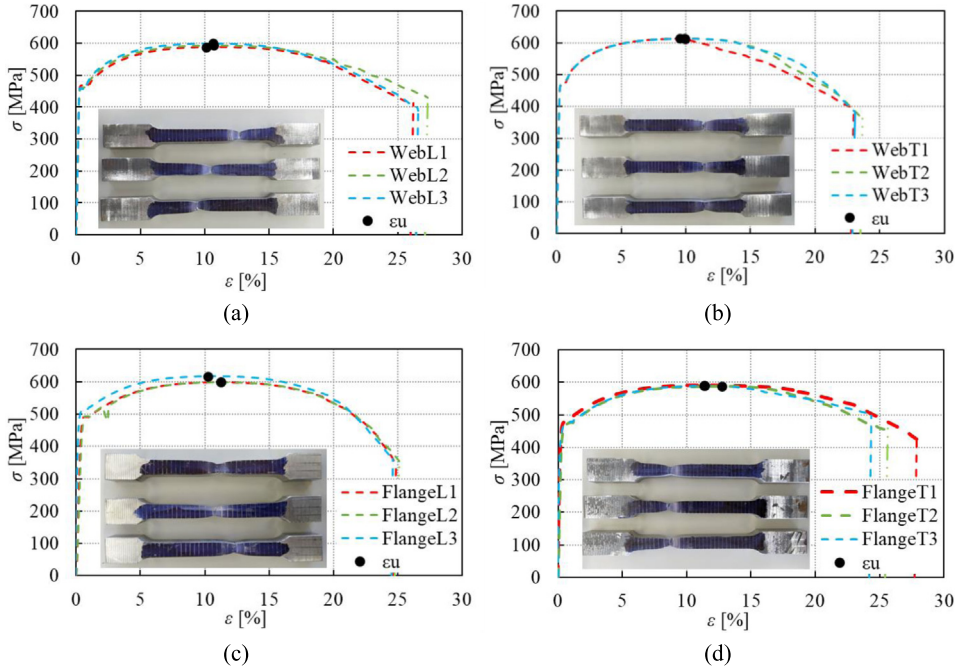

Fig. 7. Stress vs strain curves for HL1100M hot-rolled steel profile: (a) web in direction longitudinal to rolling; (b) web in direction transverse to rolling; (c) flange in direction longitudinal to rolling; (d) flange in direction transverse to rolling.

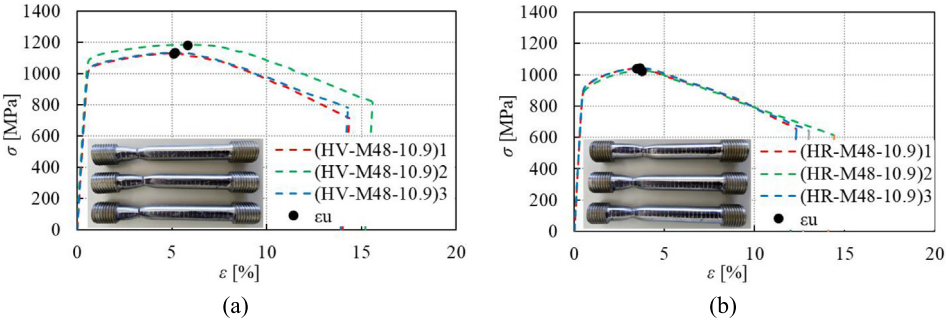

Fig. 8. Stress vs strain curves for the M48 bolts. (a) HV-M48-10.9. (b) HR-M48-10.9.

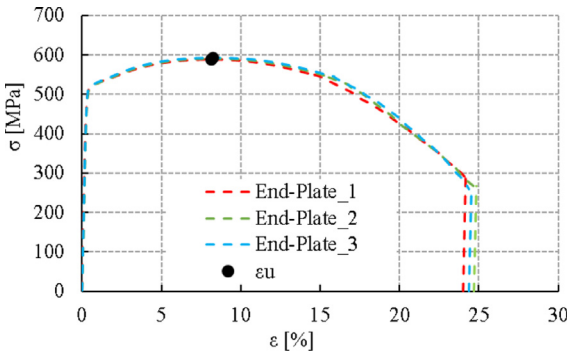

Fig. 9. Stress vs strain curves for the S460 end plates.

- An initial region in which the stiffness increases, due to the closing of gaps, bolt slipping, and other adjustment phenomena; this region is visible in the as-measured force-displacement curve Fig. 10(a) and Fig. 10(b), but has been removed in the force-displacement curve, Fig. 10(c), and in the moment-rotation curve, Fig. 10(d), that are henceforth used.
- A linear region in which the stiffness is approximately constant, up to a force $F_E \approx 2285$ kN at a displacement $D_E \approx 26.4$ mm, corresponding to a bending moment $M_F \approx 4403.8$ kN·m and a rotation $\phi_F \approx 5.2$ mrad.
- A non-linear region, corresponding to progressive yielding with increasingly reduced stiffness, up to a first peak at force $F_E \approx 3123$ kN, displacement $D_E \approx 68.3$ mm, bending moment $M_F \approx 6018.7$ kN·m, and rotation $\phi_F \approx 21.4$ mrad.
- A sudden drop in resistance, caused by the thread stripping of the HR bolts located in the first bolt row, causing a slip of the whole connection, see Fig. 10(d) and subsequent redistribution of forces between bolt rows. The resistance drops to the following values: $F_E \approx 2816.8$ kN, $M_F \approx 5428$ kN·m, measured at $D_E \approx 74.3$ mm and $\phi_F \approx 24.6$ mrad; these values are measured at the lowest point of the post-peak curve, excluding the abrupt adjustment of the jack force, which is a consequence of the displacement control and not considered as representative. Interestingly, there is only a very small increment in the displacement and rotation concerning the peak value, which is proof of the joint resilience.
- A final region in which a steady increase in strength and deformation is observed, up to a maximum displacement $D_E \approx 164.9$ mm and rotation $\phi_F = 69.6$ mrad. A high axial and bending deformation of the first bolt can be observed (Fig. 11, *B-B'*)

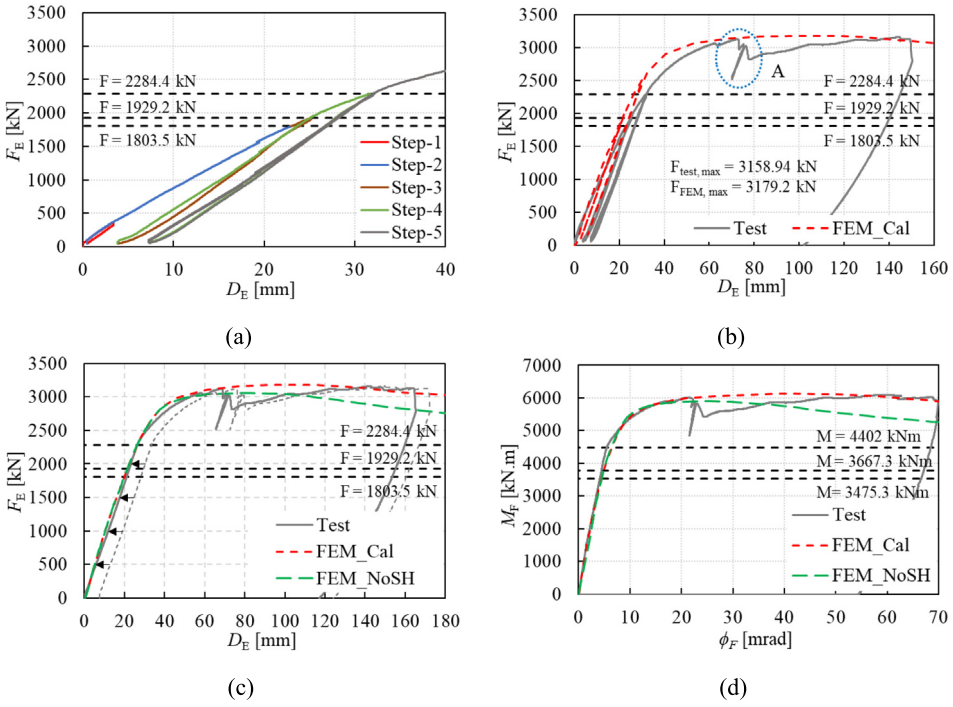

Fig. 10. Experimental and FEM curves: (a) Detail of the initial loading steps; (b) Global force vs displacement curves; (c) Force–displacement curve for step_5; (d) Moment-rotation curve for step_5.

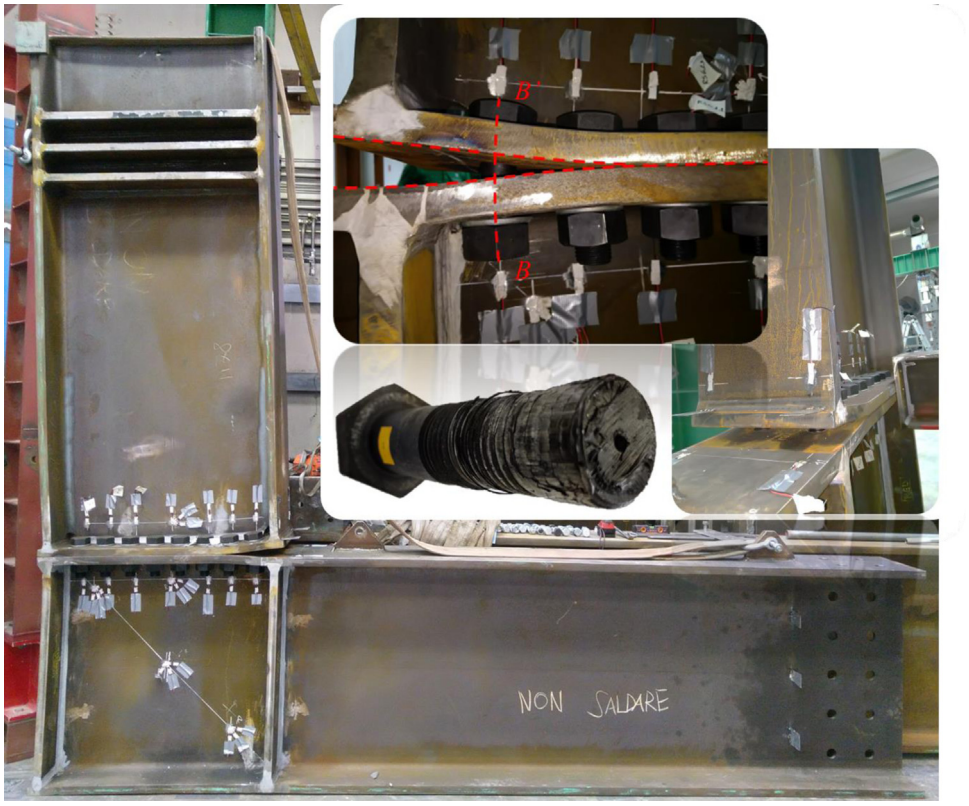

Fig. 11. Final deformed shape.

During the test, yield is detected in the column flange, end plate (very noticeable due to the scale of the test) and column web (also apparent in Fig. 11). Failure of the joint is due to the bolt thread stripping, that is, crushing of the thread allowing the nut to slip through the bolt shank, see insert on Fig. 11; this is not to be confused with a conventional bolt failure in tension. Thread stripping is not contemplated in EN 1993-1-8. Moreover, the nut for HR bolt assemblies is thicker than for HV assemblies, thus ensuring (in theory) that failure is to happen in the shank. Despite this unexpected failure mode, the moment resistance attained was 2.10 times the design bending moment.

3. Finite element models

3.1. Description of the models

To enable the full characterization of the joint behaviour and its components two detailed finite element models (FEM) using Abaqus [29] were developed:

- The first one, referred to as the validation model (or 'FEM_Cal'), used as-measured properties (including strain hardening and parallel to rolling direction) to derive the constitutive material relationship, by converting the engineering stress and strain to true stress and strain [30,31]. The adopted modulus of elasticity was 200 GPa, following the recommendations provided in prEN 1993-1-14 [32]. This model was created with the purpose of validation against the obtained experimental results, as described below.
- The second model, referred to as the verification model (or 'FEM_NoSH'), used as-measured material properties (parallel to rolling direction) with no strain hardening for the structural steel, as is usual in design. This model was created with the purpose of comparison with design rules.

The model geometry, based on nominal properties, was the same in both cases. Some images of the models are displayed in Fig. 12. The features described hereinafter are common to both models.

The idealized geometry of the large beam-to-column steel joint was considered. All parts were modelled independently and assembled specifying, where relevant, all the interactions and constraints between them. The bolts were modelled considering their effective diameter in the threaded portion so that their cross-section area coincides with the tensile stress area. The welds were not explicitly modelled because they are full-penetration butt welds. A friction coefficient of 0.2 was considered between the parts in contact. The deformability between the specimen and the reaction wall was neglected since it was monitored throughout the experimental tests and could therefore be discounted from the measured displacements as a rigid body motion. Hence, in the numerical models, the reaction wall and the Dywidag bars are not explicitly modelled.

All plate elements were meshed using first-order 3D quadrilateral (C3D8RH) and hexahedral (C3D6R) solid elements. C3D8RH is an 8-node linear brick element with reduced integration, hourglass control using the artificial stiffness method, and hybrid formulation, whereas C3D6H is a 6-node linear triangular prism, with hourglass control [29]. The mesh was chosen based on previous experience by the authors and the results of the pre-test models carried out at CERN. A final convergence study was carried out (not reported here) to ensure high accuracy. A minimum of 3 elements was considered through the thickness of each steel plate to minimize/avoid shearlocking and hourglassing [31]. However, for the endplate, 4 elements were considered through the thickness. The hexahedral element is only used to facilitate meshing in the root radius area. For different parts, different mesh sizes were selected. For instance, for the bolted steel joint, the mesh size for the bolts was 5 mm, for the end plates, supports and fixation plates 10 mm, and 40 mm for the HL1100M profile.

All contacts were modelled using the "surface-to-surface" technique, considering hard contact with "tangential behaviour" with a friction coefficient of 0.2 and a "normal behaviour" considering "hard" contact for the pressure overclosure and allowing the separation after contact.

As mentioned, the bolts were modelled with nominal geometrical properties, except that the bolt shank diameter was based on the bolt tensile area. The preload was applied by using the bolt-load option in Abaqus. As mentioned, the applied bolt pre-load was 930 kN for the bolted joint.

The boundary conditions were as similar as possible to those of the experimental tests. The specimen was fixed to the reaction wall using the auxiliary stiffened angles. Additionally, a simple support was also positioned at the corner of the joint.

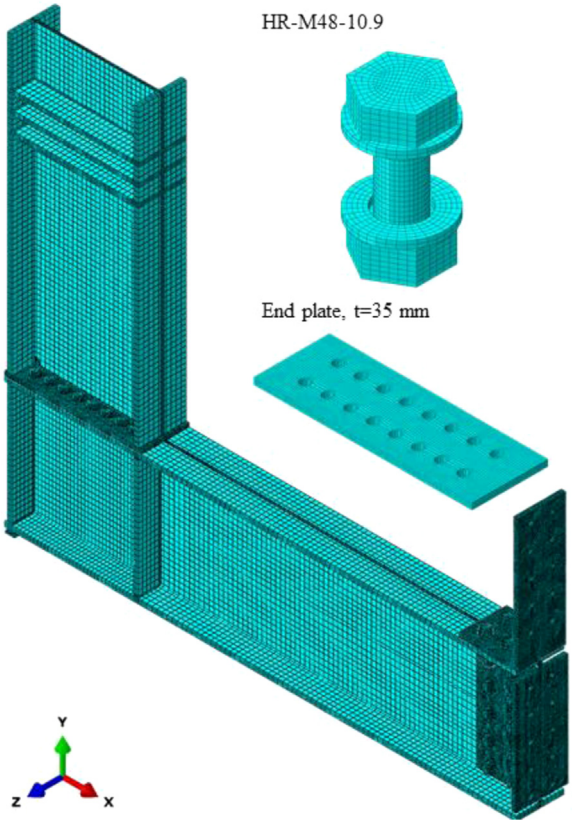

Fig. 12. General view of the FEM model including details of end plate and bolt mesh.

The loading protocol of the FEM models resembled that of the test. The measured test displacements were used as displacement targets for the analysis.

It is worth mentioning that to perform a detailed analysis of the developed models aiming to individualize the contribution of all relevant components it is necessary to request *NFORC* (forces at the nodes of the element caused by the stress in the element) for solid elements to adequately perform free-body cuts.

3.2. Validation of the models

The FEM_Cal model results show a good agreement with the experimental results. Fig. 13 shows a qualitative comparison of the joint deformation between the test and FEM models. The main trends observed in the former are present in the latter, namely: (i) large rotation of the beam with respect to the column; (ii) local yielding of column flange in the proximity of the first bolt row; (iii) local yielding of end plate in the proximity of the second bolt row; (iv) shear yielding of the column web, visible through the rhomboidal distortion of the web panel. The large scale of the test makes all these deformations easily perceptible to the naked eye. The column rotation is clearly very small in comparison to the joint rotation.

Fig. 10(c) and Fig. 10(d) show the force–displacement and moment–rotation curves obtained from the FEM, superimposed with the experimental ones. An excellent coincidence is observed up to the point of thread slipping. Comparisons between the test and the FEM displacements at the local level, shown in Fig. 14, also display an outstanding coincidence, indicating that the FEM correctly reproduces the behaviour of the test. Therefore, this FEM can be reliably used to obtain extra information about the joint, not directly available from the test. This feature makes it an excellent tool to overcome some of the inherent limitations in the test instrumentation, on the condition of previous validation of key parameters.

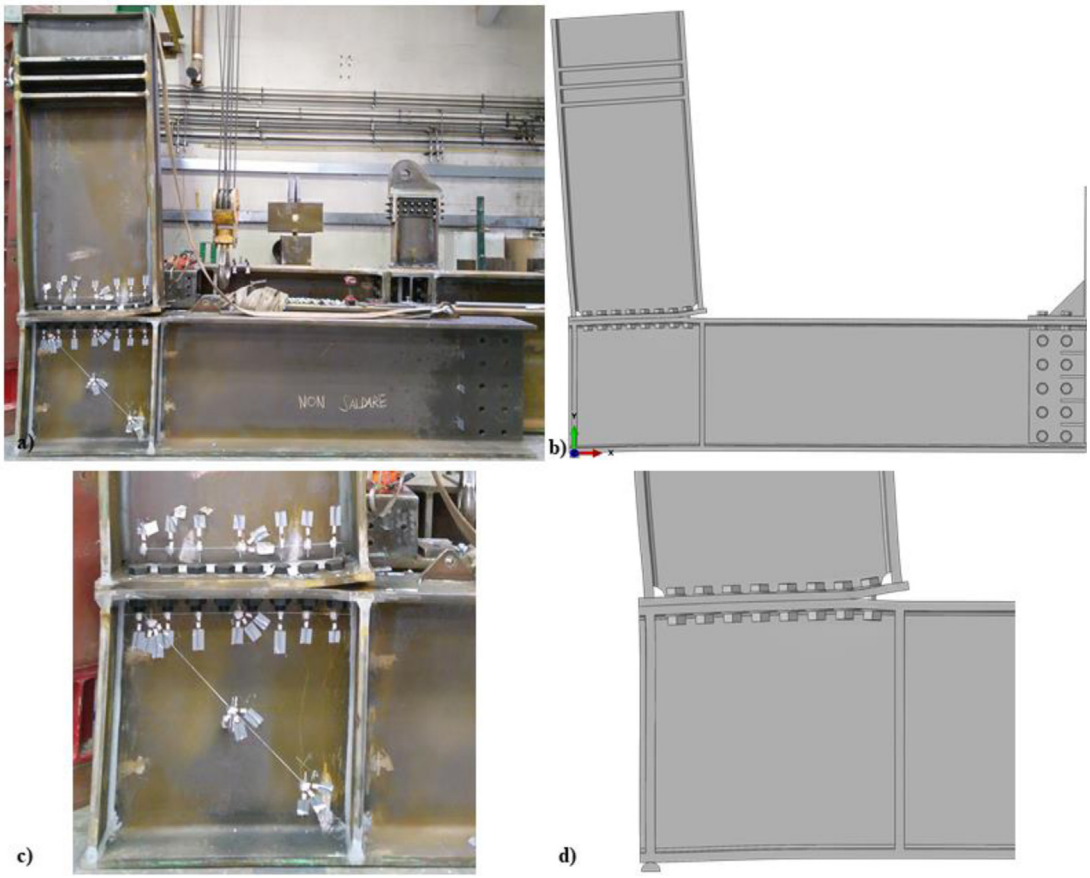

Fig. 13. Qualitative comparison of joint deformability in test vs FEM: (a) global deformation in the test; (b) global deformation in FEM; (c) local deformation in the test; (d) local deformation in FEM.

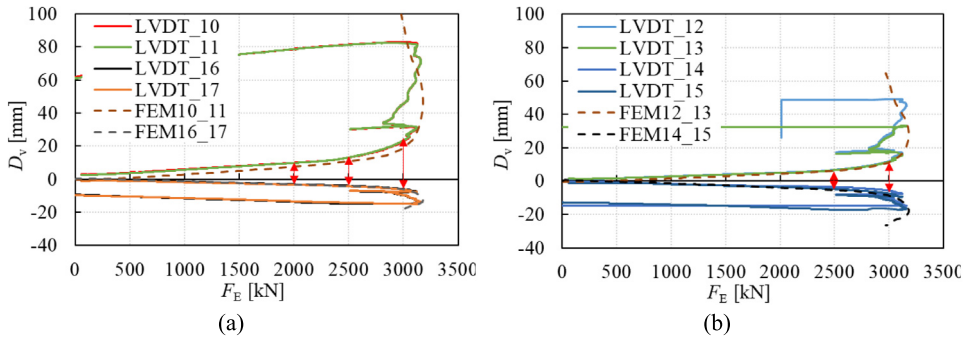

Fig. 14. Quantitative comparison of local displacements in test vs FEM: (a) vertical displacements; (b) horizontal displacements.

3.3. Detailed FEM results

The calibration model described in the previous sections is successful in simulating the real structural behaviour of the test. However, this model is not suitable to characterize the joint resistance and stiffness from the perspective of Eurocode 3, whereby design resistance is mostly based on yield strength values. For this reason, a new FEM model has been developed, in which the material model is elastic-perfectly-plastic, i.e., strain hardening is omitted. The yield strength considered was the minimum averaged experimental value (f_y = 464 MPa for S460ML, f_{yb} = 921 MPa for all bolts). In all other aspects, this model resembles the validation model (FEM_Cal). This FEM (referred to hereby as 'FEM_NoSH') allows a consistent comparison of results with those of the component method (CM).

Some results of this model for relevant connection parts are shown graphically in Fig. 15 (end plate), Fig. 16 (column flange) and Fig. 17 (column web). The term 'part' is not to be confused with the term 'component'. The former is a geometrically defined unit, such as end plate, column flange, column web panel or bolt. The term 'component' refers to the specific behaviour of a part related to a bolt row, such as end plate in bending (EPB), bolt in tension (BT), column flange in bending (CFB), column web in tension (CWT) or column web in shear (CWS). The selected results for the parts include Von Mises stress σ_{VM}, equivalent plastic strain $\varepsilon_{p,eq}$, and one significant stress field for each part, at the following values of the applied bending moment M_F:

- No moment, $M_F = 0$, shown only for the end plate (Fig. 15). At this stage only the bolt pre-load effect is visible.
- Onset of yielding of the relevant part (elastic behaviour) $M_{F,e,part}$, identified as the load step for which the part features no equivalent plastic strain, $\varepsilon_{pl,eq} = 0$. This load step is part-dependent, and

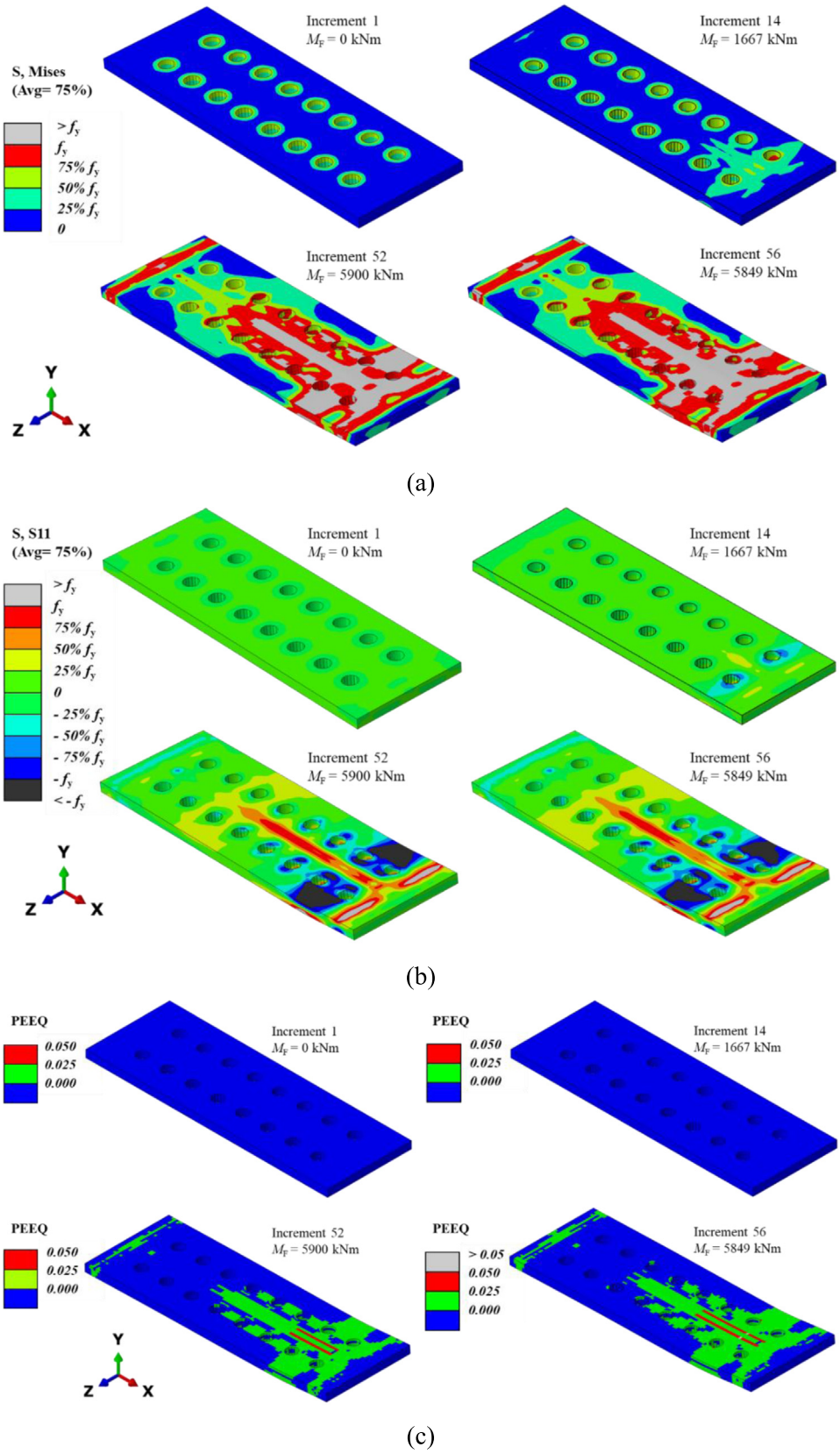

Fig. 15. End plate stress and strain at different applied bending moments: (a) Von Mises σ_{VM}; (b) stress component σ_x; (c) Equivalent plastic strain $\varepsilon_{p,eq}$.

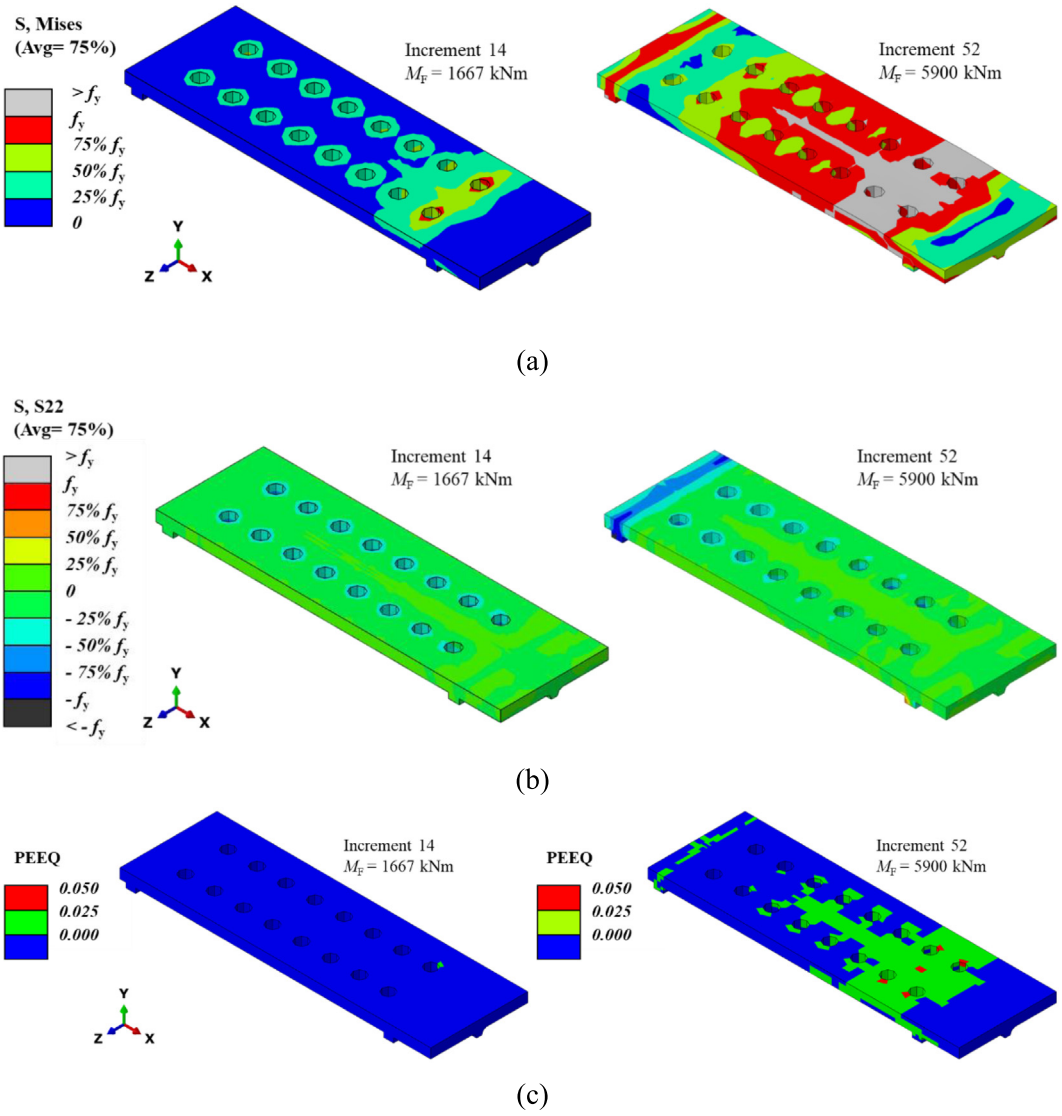

Fig. 16. Column flange stress and strain at different applied bending moments: (a) Von Mises σ_{VM}; (b) stress component σ_x; (c) Equivalent plastic strain $\varepsilon_{p,eq}$.

the lowest value for all parts identifies the onset of yielding for the whole joint, $M_{F,e}$.

- Maximum acceptable strain for the relevant component and bolt row r, $M_{F,lim,r}$ identified as the load step for which the component features an equivalent plastic strain $\varepsilon_{pl,eq} = \varepsilon_{pl,lim}$, where $\varepsilon_{pl,lim}$ is adopted as 5% in general and 2.3% for the bolts, as per prEN 1993-1-14. This load step is component- and bolt-row-dependent and the lowest value for all components and bolt rows identifies the maximum acceptable load step for the joint $M_{F,lim}$.
- Maximum resistance of the joint, $M_{F,max}$ = 5900 kN·m, defined as the peak value in the moment-rotation curve. The corresponding rotation value is $\phi_{F,max}$ = 28.55 mrad.

3.4. Extraction of individual component behaviour from FEM

To perform meaningful comparisons with the component method, the individual component behaviours must be isolated. The following methodology is adopted:

3.4.1. Column shear

To obtain the column shear V_r at bolt row r, the column is first isolated from the set and then cut by 8 consecutive transverse planes (orthogonal to the column axis), each of them located at midpoint between bolt axes, as shown in Fig. 18(a) where the bolt row axis are indicated with an 'r' (r_1, r_2,… r_8) and the cutting plane positions are indicated with a 'c' (c_1, c_2,… c_8). The free body cut isolating either side of cut r yields the column shear V_r at that point of the column axis. There is no need to produce a cut to the right of bolt row 1, because the shear at that section is $V_0 = V_c = N$. Shear forces are considered as positive when they act as shown in Fig. 18(b).

3.4.2. Bolt row forces

The subtraction of two consecutive values of shear at cuts r-1 and r is the force F_r at bolt row r, as indicated by the free body equilibrium in Fig. 18(b). This force includes the effect of prying forces and is, therefore, smaller than the sum of the two bolt forces at row r, $F_{BT,r}$, where subscript 'BT' stands for component 'bolt in tension'. The prying forces $F_{Pry,r}$ can be found by subtracting the bolt row force from the bolt force.

3.4.3. Component deformation

The individual component deformation of bolt row r can be calculated accurately by extracting the nodal displacements of 5 control points A, B, C, D, F, situated in successive cross-sections aligned with the bolt rows, represented generically in Fig. 18(c). Points A, D and F are on the connection's axis of symmetry and located, respectively,

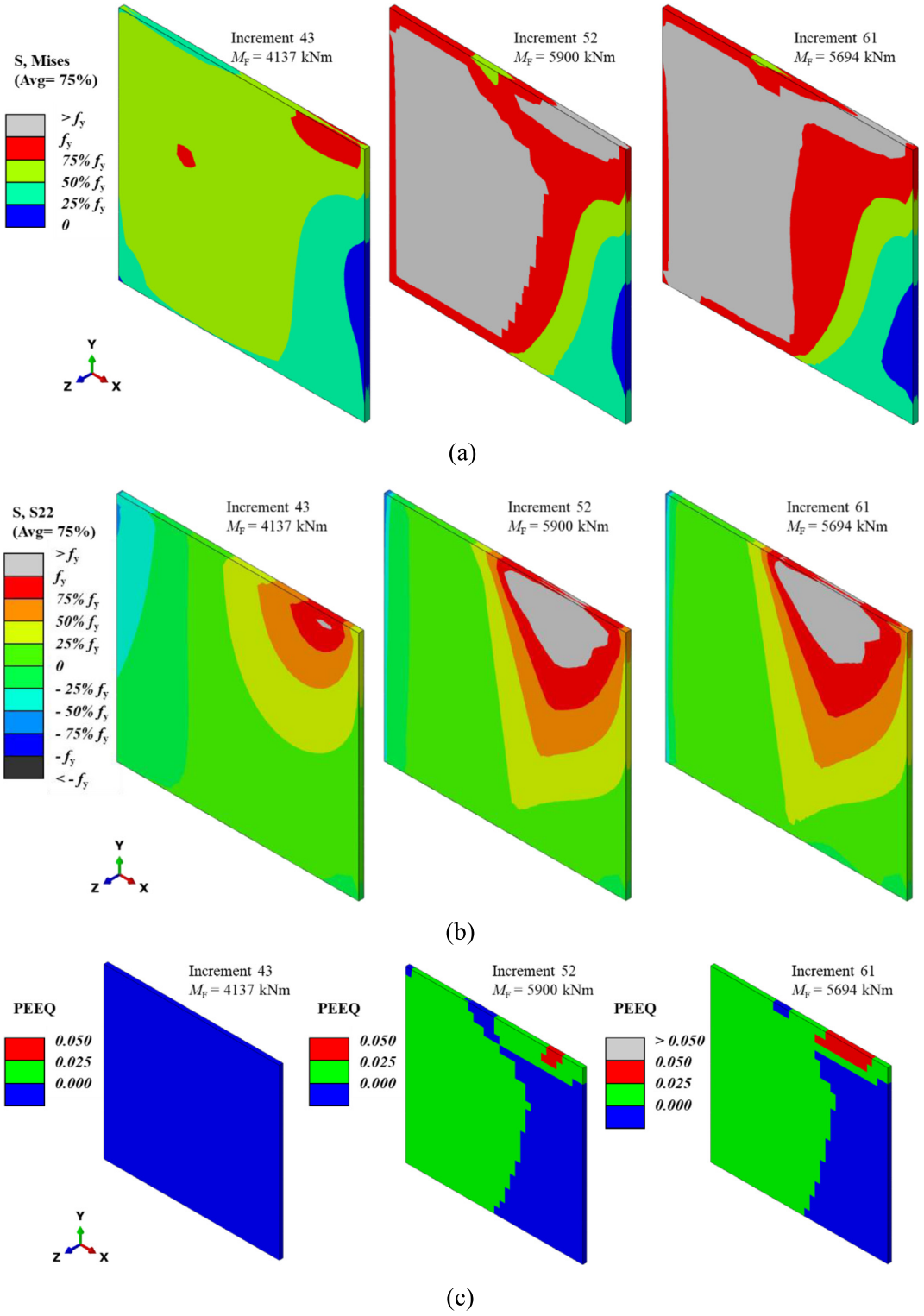

Fig. 17. Column web stress and strain at different applied bending moments: (a) Von Mises σ_{VM}; (b) stress component σ_y; (c) Equivalent plastic strain $\epsilon_{p,eq}$.

at the intersection of the beam web with the end plate (point A), and root radius end at both sides of web (points D and F), with point D closest to the connection. Points B and C are located at the theoretical intersection of the bolt axis with the end plate (point B) and inner side of the column flange (point C). In fact, two positions exist for each one of these points, as there is one bolt at either side of the beam web, so the average displacement for both is extracted. An extra control point E is added at the column axis to obtain an intermediate value of column web deformation. The component displacement is given by:

$$\Delta_{EPB,r} = u_{A,r} - u_{B,r}, \tag{5}$$

$$\Delta_{BT,r} = u_{B,r} - u_{C,r}, \tag{6}$$

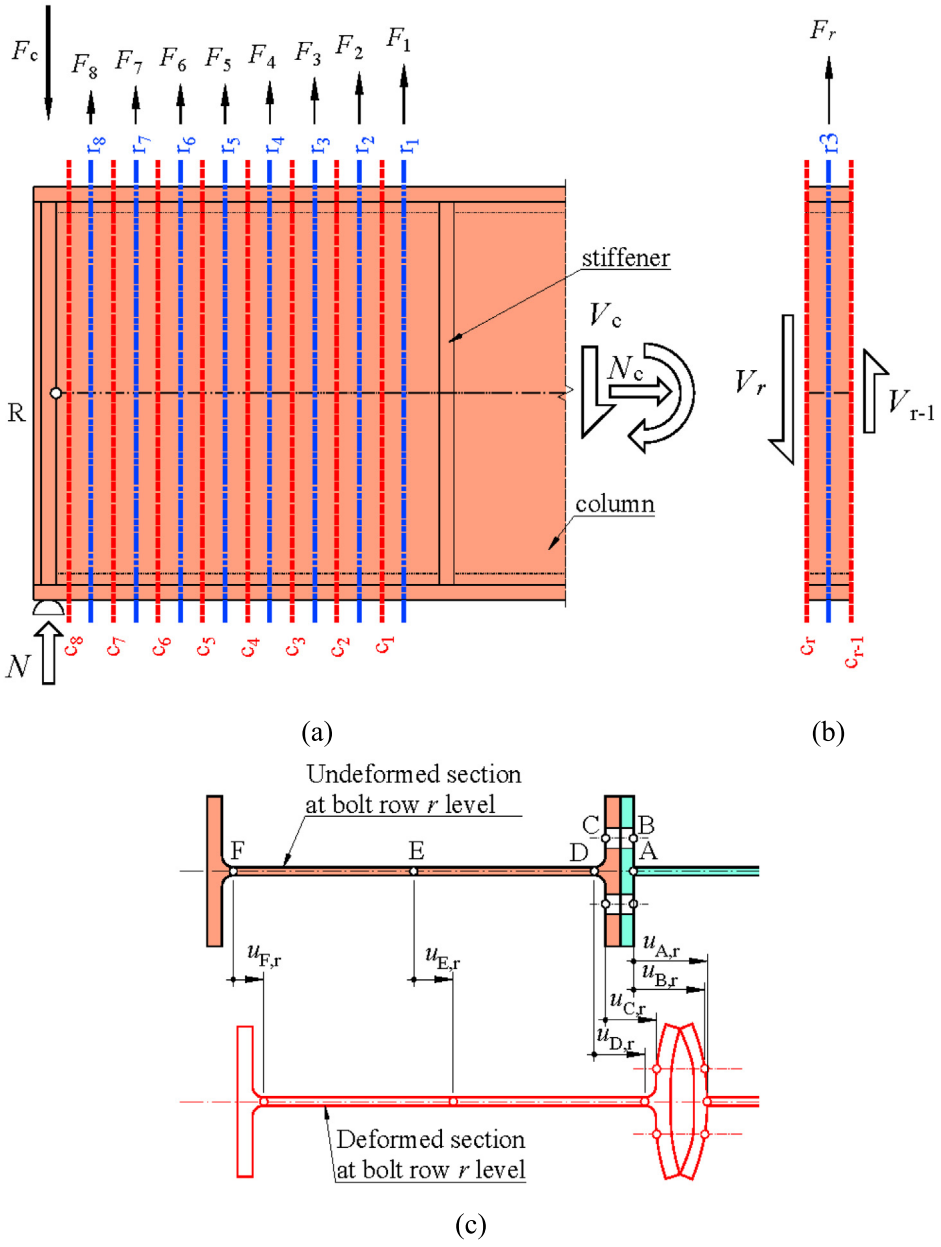

Fig. 18. Section cut procedure: (a) section cut definition; (b) free-body diagram to isolate row bolt force; (c) component deformation extraction.

$$\Delta_{\mathrm{CFB},} = u_{\mathrm{C},r} - u_{\mathrm{D},r}, \tag{7}$$

$$\Delta_{\mathrm{CWT},r} = u_{\mathrm{D},r} - u_{\mathrm{F},r}, \tag{8}$$

$$\Delta_{\mathrm{CWS},r} = u_{\mathrm{F},r}, \tag{9}$$

where $u_{\mathrm{A,r}}$, $u_{\mathrm{B,r}}$, $u_{\mathrm{C,r}}$, $u_{\mathrm{D,r}}$, $u_{\mathrm{F,r}}$ are the total 'corrected' displacements at control points A, B, C, D, F, respectively, and the subscripts indicate the component (listed again here for convenience, EPB = End Plate in Bending, BT = Bolt in Tension, CFB = Column Flange in Bending, CWT = Column Web in Tension, CWS = Column Web in Shear) and row number. The term 'corrected' displacement indicates that u is measured parallel to the column web, as shown in Fig. 18(c), by removal of rigid body motion components due to rotations and displacements measured at the point of intersection (point R) of the column axis with the left stiffener, see Fig. 18(a). For the CWS, the meaningful variables are bolt row shear (instead of bolt row force), and angular distortion (instead of displacement). The latter can be expressed as

$$\gamma_{\mathrm{CWS},r} \approx \frac{\Delta_{\mathrm{CWS},r} - \Delta_{\mathrm{CWS},r-1}}{s_r} = \frac{\Delta_{\mathrm{CWS},r} - \Delta_{\mathrm{CWS},r-1}}{z_r - z_{r-1}}, \tag{10}$$

where s_r is the sub-panel width and z_r the sub-panel lever arm to the nominal compression centre of the joint, (line of action of both N and F_c in Fig. 18). The corrected displacements and the component displacements obtained from Eqs. (5)–(9) at the maximum load reached in the FEM_NoSH ($M_{\mathrm{F,max}}$ = 5900 kN·m, $\phi_{\mathrm{F,max}}$ = 28.55 mrad) are plotted in Fig. 19(a)–(b), where the order of bolt rows advances from right to left, with bolt row 1 located on the right side (z_1 = 954 mm). In the component plot, the first bolt yielding is evident. The deformation due to the column web is larger than for any other component, and the largest deformation for all components (excluding BT) occurs for the second bolt row. Additionally, the corrected displacements and component displacements are plotted for the last elastic load step in Fig. 19(c)–(d). The determination of the load step for which the behaviour is elastic is explained in the next sub-section.

Fig. 19(a) shows that the first bolt row presents a larger displacement than the rest. However, this deformation is not equally distributed between the different components. Because the bolts at the first bolt row are totally yielded at an early load stage, they provide the deformation needed for compatibility; thus, the other individual components

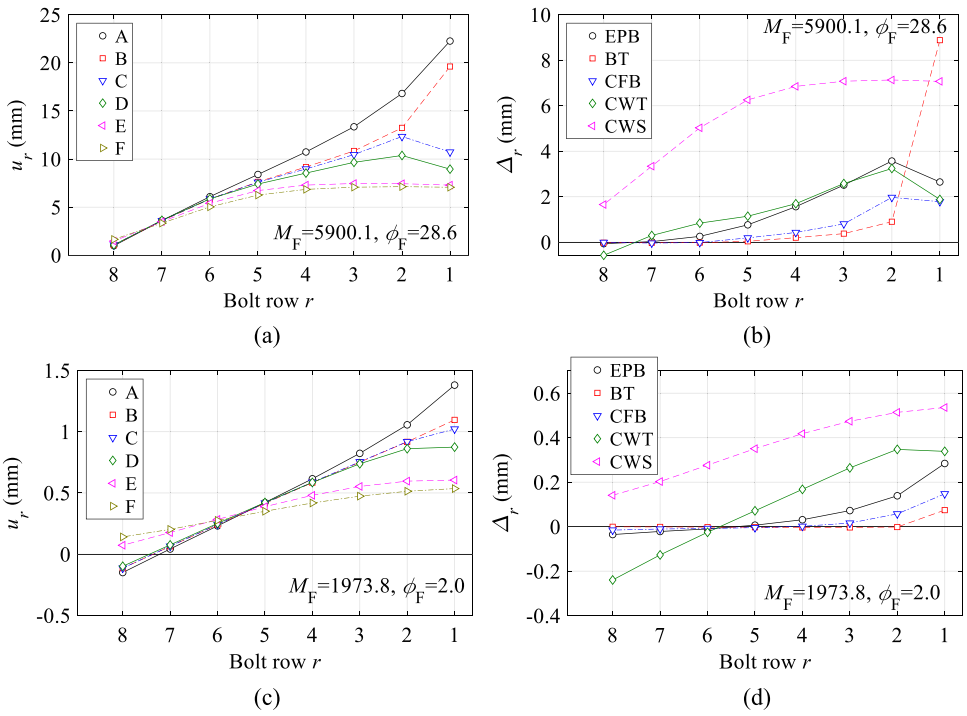

Fig. 19. Component corrected displacements: (a) total at $M_{F,max}$; (b) component at $M_{F,max}$; (c) total at $M_{F,e}$; (d) component at $M_{F,e}$.

(EPB, CFB, CWT) remain at the deformation corresponding to a lower load level. For this reason, Fig. 19(b) shows a decrease in deformation between bolt rows 2 and 1 for all the components except the bolts (BT), that show a conspicuous increase.

3.4.4. Limiting strain

The values of moment and rotation limited by the component equivalent plastic strain are listed in Table 4. The identification of the loading step for which $\varepsilon_{pl,lim}$ is reached is done in the following way: a sub-set of elements corresponding to the part of the component isolated between cuts c_{r-1} and c_r (see Fig. 18(a)) is selected; the loading steps are examined, until the first step for which $\varepsilon_{pl,eq}$ obtained at the integration point for any element in the sub-set is larger than or equal to $\varepsilon_{pl,lim}$. This process permits also the identification of the last step for which the component remains fully elastic as the last step for which $\varepsilon_{pl,eq} = 0$. Regarding the bolts in tension (BT), two sets of values are listed: column $BT_{2.3\%}$ corresponds to a $\varepsilon_{pl,lim} = 2.3\%$ and column $BT_{5\%}$ corresponds to $\varepsilon_{pl,lim} = 5\%$. The values for which the component is limiting (rotation $\phi_{F,lim,r} < \phi_{F,max}$) are marked with an asterisk (*), and correspond to the bolts in tension component. If the standard 2.3% limit is adopted, the limit rotation imposed by the first bolt row would be $\phi_{F,lim,1} = 6.0$ mrad, which increases to 8.2 mrad if a 5% limit for the bolt is allowed. These theoretical rotation limits are much lower than the experimental rotation. For the thread stripping point the rotation is already larger than 20 mrad. The reason might be in the type of bolt failure observed: whereas the expected BT component behaviour is purely in tension, compatibility with the gripped plates results in shank curvature and therefore bending (see insert in Fig. 11), which produces high local plastic strain at early load levels. All other components reach their limiting plastic strain at rotations higher than $\phi_{F,max}$, and in fact the limiting plastic strain is not reached for CFB and CWS at any bolt row. Bolt rows 6, 7 and 8 are not limiting. If the bolts are excluded, the limiting component becomes the end plate in bending, for which the limiting rotation is 40.7 mrad at the second bolt row, corresponding to 143% of $\phi_{F,max}$.

Force–deformation plots for each individual component and bolt rows 1 to 7 are shown in Fig. 20. Bolt row 8 is excluded because it is in compression for the whole range of load applications. Bolt row 7 is initially in compression and gradually enters the tension realm. For all components bolt row force F_r is plotted vs. component displacement Δ, except for CWS where bolt row shear V_r is plotted vs. angular distortion $\gamma_{CWS,r}$, see Fig. 20(d). For BT an additional plot is presented with the bolt row force F_r replaced by the bolt force $F_{BT,r}$, which includes prying forces and preload (1860 kN per bolt row). On the plots, each line corresponds to a different bolt row r. An additional marker indicates the point in the curve where the component reaches an equivalent plastic strain $\varepsilon_{pl,eq}$ equal to a limiting value $\varepsilon_{pl,lim}$, chosen according to prEN 1993-1-14 [31]. The curves beyond this limiting value are shown in thin dotted lines. If the marker is omitted, it is indicative that the component does not reach $\varepsilon_{pl,lim}$. This is the case for components CFB and CWS.

The steps for which the components and bolt rows reach $\varepsilon_{pl,lim}$ are identified on the global moment–rotation curve in Fig. 21. For all cases, the corresponding points are located to the right of the peak bending moment, except for the component BT in bolt rows 1 and 2. Comparison with the real test (Fig. 10) shows that the 2.3% limit set by prEN 1993-1-14 for the bolts is too conservative. In fact, the real material curves shown in Fig. 8(b) display a plastic strain of about 3.5% at tensile load. If the 2.3% limit for the first bolt is considered, the moment resistance of the joint cannot exceed 4137 kN·m, which is 70% of the maximum moment according to the FEM_NoSH and 67% of the maximum moment according to the test results (before bolt stripping).

3.4.5. Shear distribution

The shear force carried by different cross-section regions of the column can be found isolating these regions from the model and repeating the section cut process. This is done for two different regions in the joint: (i) the panel zone region, identified as the flat part of the column web, with cross-section area $A_{pzc} = d_c \cdot t_{wc}$, where $d_c = 968$ mm is the depth of the web flat and $t_{wc} = 22$ mm is the web thickness; (ii) the column flange region, identified as the part of the column not included in the panel zone, with area $A_{frc} = A_c - A_{dc}$, where A_c is the total column cross-sectional area. The code-defined shear area A_{vz} is a notional area, so the identification with a specific region of the section does not make sense from a mechanical point of view. The shear values obtained at bolt row r are referred to as $V_{pzc,r}$ and $V_{frc,r}$. The

Table 4
Values of moment and rotation limited by component equivalent plastic strain.

	Bolt row r	EPB	$BT_{2.3\%}$	$BT_{5\%}$	CFB	CWT	CWS
Values at onset of yielding							
Rotation $\phi_{F,e,part}$ (mrad)	All	1.65	0.56	0.56	1.65	3.06	7.53
Moment $M_{F,e,part}$ (kN·m)	All	1667.1	631.8	631.8	1667.1	2801.8	4983.3
Values limited by max. strain $\epsilon_{pl,eq} = \epsilon_{pl,lim}$							
Rotation $\phi_{F,lim,r}$ (mrad)	1	46.1	[a]6.0	[a]8.2	N.R.	77.4	N.R.
	2	40.7	[a]20.1	40.7		52.7	
	3	48.2	40.7	85.6		58.2	
	4	70.2	40.7				
	5	N.R.	61.9	N.R.		N.R.	
	6, 7, 8		N.R.				
Moment $M_{F,lim,r}$ (kN·mm)	1	5791.5	[a]4428.8	[a]5177.6	N.R.	5322.2	N.R.
	2	5849.1	[a]5853.4	5849.1		5694.2	
	3	5762.9	5849.1	5215.5		5598.4	
	4	5418.2	5849.1				
	5	N.R.	5536.7	N.R.		N.R.	
	6, 7, 8		N.R.				

N.R. indicates that the limiting value is not reached for this component during the analysis.
[a]*Indicates that the corresponding value is below the resistance value.*

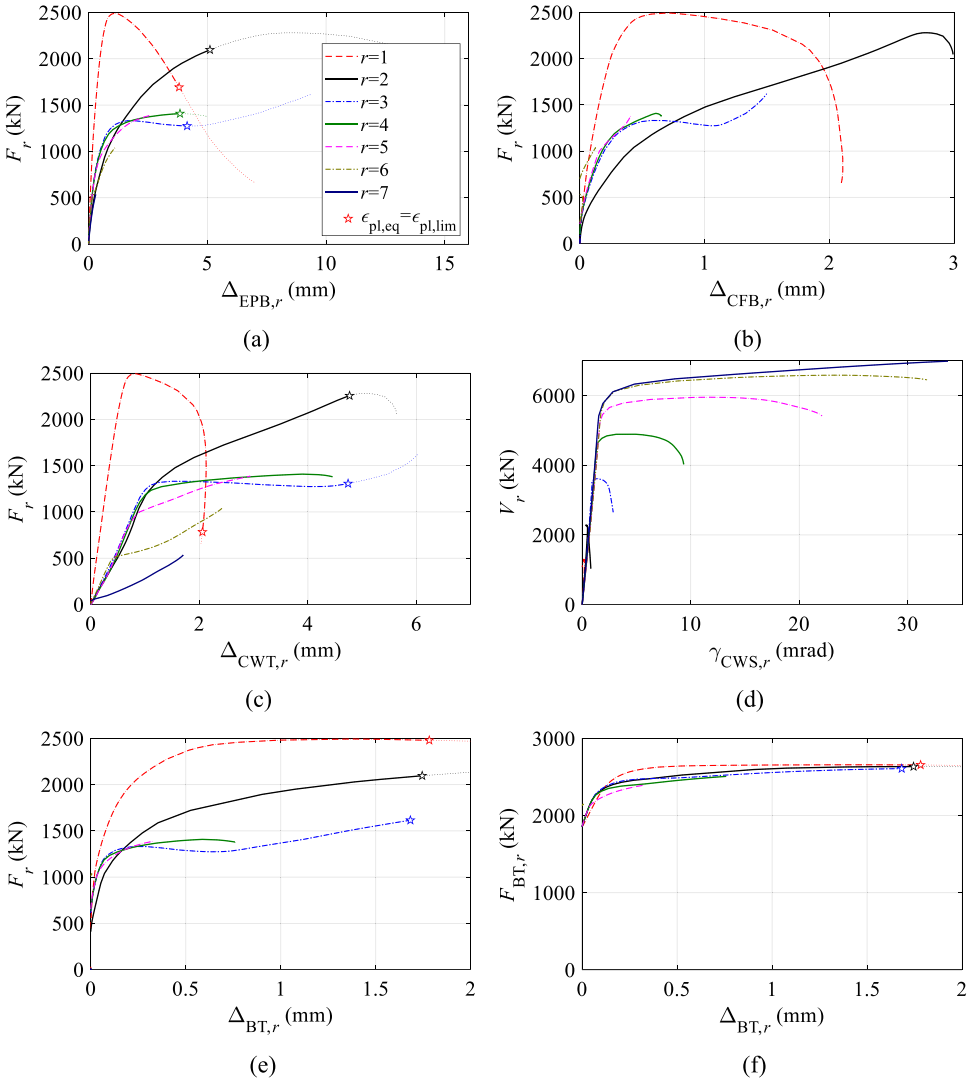

Fig. 20. Force–deformation plots of individual components: (a) EPB; (b) CFB; (c) CWT; (d) CWS; (e)(f) BT.

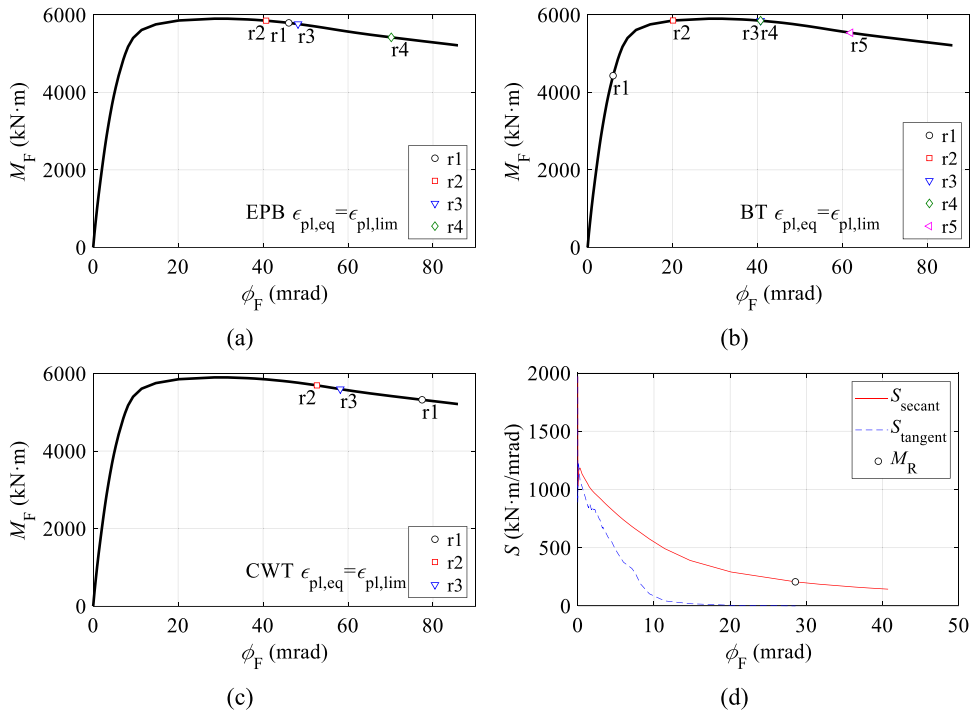

Fig. 21. Moment–rotation curves with identification of failure point of individual bolt row components: (a) EPB; (b) BT; (c) CWT.

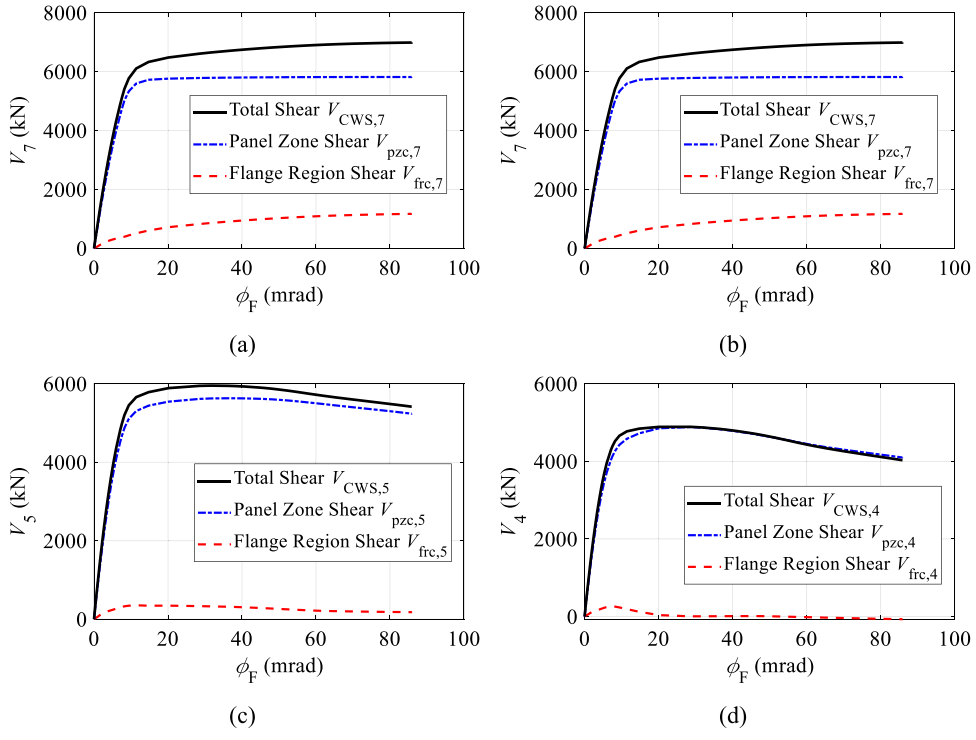

Fig. 22. Shear at column web, panel zone and flange region: (a) bolt row 7; (b) bolt row 6; (c) bolt row 5; (d) bolt row 4.

two values add up to the total shear V_r. Fig. 22 shows the evolution during loading of the three shear forces for bolt rows 4, 5, 6 and 7. For bolt rows 7 and 6, Fig. 22(a)–(b), the panel zone is fully yielded, as shown by the totally horizontal tail of the corresponding curves. The flange region contribution increases non-linearly with joint rotation up to approximately 40 mrad; after that, the behaviour differs between bolt rows 6 and 7. In the former, the flange region contribution reaches a plateau, indicating full yield, whereas in bolt row 7 the contribution increases steadily up to the end of loading. For bolt row 5 and 4 the flange region contribution is small.

4. Component model

4.1. Introduction

The component method is a well-established and simple procedure to assess the resistance and stiffness of steel joints [4]. The method

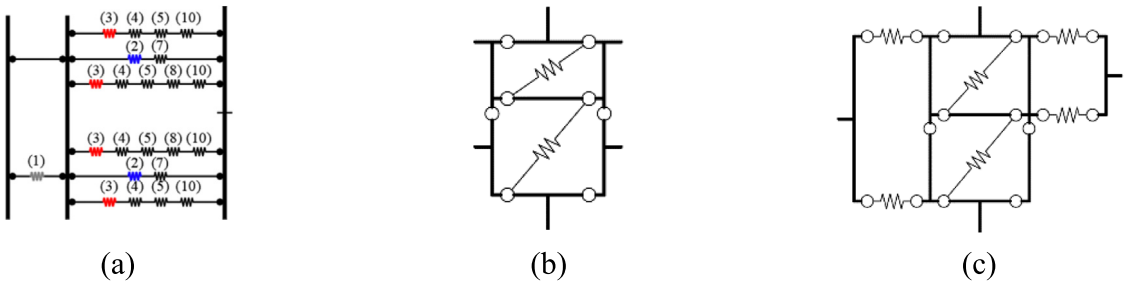

Fig. 23. Component models for specific beam-to-column joints: (a) beam-to-column joints subject to bending and axial force [33]; (b) Internal node (composite joints) [34]; (c) internal node (steel joints, beams of unequal depth) [35].

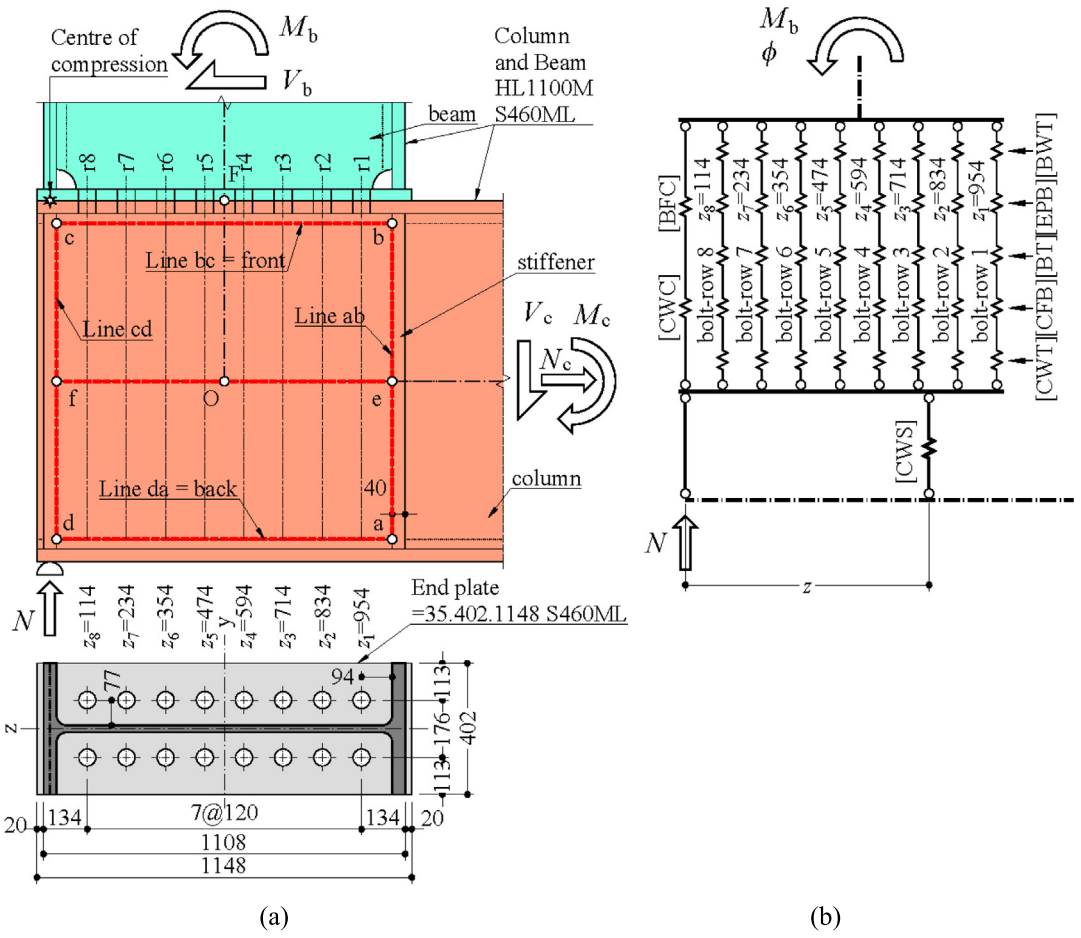

Fig. 24. Model of joint C2: (a) geometry; (b) component model.

is based on research efforts carried out mainly in Europe and is fully integrated in Eurocode EN 1993-1-8 [11]. The method is based on the identification of the joint basic active components, the subsequent assessment of their force–displacement characteristics and finally by assembling the individual properties of these components using appropriate rigid links and linear spring component models, Fig. 23. A detailed explanation of the component method can be found in [4].

In simple cases, such as welded joints or bolted flush end-plate beam-to-column joints with a single bolt row in tension, the component model is statically determinate, leading to a straightforward calculation of the rotation of the joint and the applied forces and deformation in each component using only equilibrium conditions. However, for bolted joints with multiple bolt rows in tension or more complex welded joint typologies such as an internal node beam-to-column joint connecting two beams of unequal depth [35], the component model becomes statically indeterminate, and its solution requires compatibility conditions in addition to the equilibrium equations. Fig. 24(b) exemplifies such a case, depicting a component model applicable to joint C2, with 8 bolt rows, that requires a simple numerical solution to obtain the initial stiffness of the joint.

To allow for a simple hand calculation in the case of joints in bending, EN 1993-1-8 [11] proposes a simplified methodology whereby the component model is transformed into an equivalent static determinate model by implementing the following step-by-step procedure [36]:

(i) Assembly of all springs in a bolt row into a single equivalent spring: equivalent spring in series in tension for bolt row r.
(ii) Assembly of all springs in the compression zone into a single equivalent spring: equivalent spring in series in compression.
(iii) Assembly of all equivalent springs in tension for all bolt rows into a single global equivalent spring for the tension zone: equivalent spring in parallel in tension.

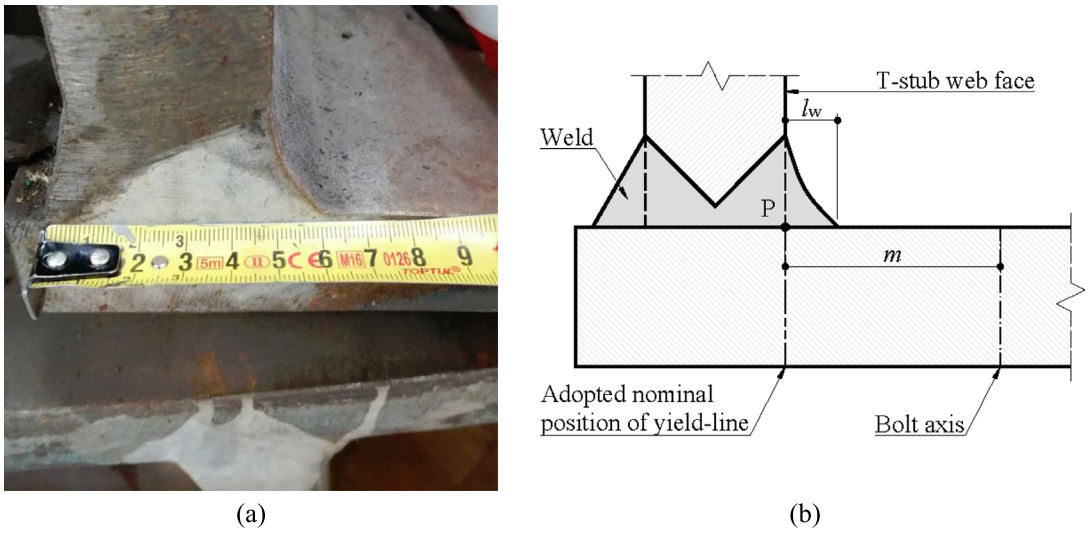

Fig. 25. Butt welds with superimposed fillet welds: (a) specimen; (b) assumed position of yield-line.

(iv) Solution of the equivalent statically determinate component model using only the equilibrium conditions.

Alternative component models may be established that are appropriate for specific joint typologies, see Fig. 23 or to provide a more general model that is able to deal with fire [37], cyclic [38] loading or a generic 3D node [39].

For large joints with many bolt rows, the subdivision of the component web panel in shear into several sub-components aligned with the various bolt rows seems to bring additional accuracy to the prediction of joint behaviour. It was successfully proposed to deal with composite joints (Fig. 23(b)) and beam-to-column joints with beams of unequal depth (Fig. 23(c)) and recently also applied to standard steel joints [40].

In the following sub-sections, the component method will be applied to joint C2.

4.2. Application of the simplified component model of eurocode 3

The geometrical definition for joint C2 is shown in Fig. 24(a), whereas the corresponding component model according to EN 1993-1-8 is presented in Fig. 24(b). The different components are identified with abbreviations in brackets (e.g., [CWT]); the joint is composed of 2 parts: (i) the connection and (ii) the column web panel. The column web panel comprises 3 distinct components: the column web panel in shear [CWS], the column web in compression [CWC] and the column web in tension [CWT]. For the calculation of stiffness, the CWC can be dismissed in this case, due to the presence of a double-sided stiffener aligned with the centre of compression with cross-section approximately equal to that of the beam flange. The connection presents 8 bolt-rows, each of them comprising 4 different active components: column flange in bending [CFB], bolts in tension [BT], end plate in bending [EPB] and beam web in tension [BWT]. The tension in the bolt rows must be balanced by compression in the beam top flange and web [BFC], compression in the column web [CWC], and cannot be larger than the column web panel shear resistance [CWS] excluding the fraction needed to resist the column shear. Welds are assumed as full-penetration and can be neglected in the verification. The design resistance and initial stiffness of each component can be found with well-known expressions in EN 1993-1-8 [11]; for some components, these properties are obtained by analogy with a T-stub of notional length. For the strength evaluation, the minimum averaged as-measured material properties are adopted (f_y = 464 MPa, f_u = 589 MPa for S460ML; f_{yb} = 921 MPa, f_{ub} = 1036 MPa for grade 10.9 bolts), without considering partial factors. Nominal geometrical properties are considered. EN 1993-1-8 does not contain rules to calculate the design resistance for the CWC in the case of a stiffened column web. Hereby, the resistance of this component is calculated assuming an effective contributing width of stiffener and column web of $b_{eff} = 10{\cdot}\varepsilon{\cdot}t$, measured from the intersection axis between column web and stiffener, where $\varepsilon = (235\ \text{MPa}/f_y)^{0.5}$, and t is the plate thickness of the corresponding part, column web ($t = t_{wc}$ = 22 mm) or stiffener ($t = t_s$ = 40 mm).

The relationship between the forces presented in Fig. 5(a) and those in Fig. 24(a) is: $V_b = N_c = F_E$. The values of the bending moment on the beam and on the column are dependent on the point chosen; in this analysis, M_b is the bending moment acting on the connection (i.e., $M_b = M_F$), and M_c is measured at point C (i.e., $M_c = M_C = M_b - N{\cdot}(h_b - t_{fb}/2)$, where h_b is the beam depth and t_{fb} the beam flange thickness). This is of special importance due to the size of the joint. As shown in Table 1, the bending moment measured at point O is 129% the value at point F.

To evaluate the resistance of the components involving plate bending, the yield line to bolt axis distance on the notional T-stub is critical and depends on the root radius or weld between the flange and the web of the T-stub. The specimen presents butt welds reinforced by superimposed fillet welds with a leg l_w of approximately 20 mm for the web and 10 mm for the flange. No exact rules exist for the determination of the position of the yield line for this weld typology. Hereby, the yield line is assumed at the theoretical intersection of flange and web, as shown in Fig. 25. This position is consistent with the FE model.

The resistance of the individual components is listed in Table 5. The weakest component on each bolt row, highlighted in the table, controls its behaviour. Three different scenarios are presented: (A) excluding the reaction force N; (B) including N and assuming the column base as pin-jointed; (C) including N and assuming the column base as fixed. The purpose of the first analysis (A) is simply to assess the relevance of N on the joint resistance. In the second (B) and third (C) analyses, the procedure must be carried out iteratively because N is dependent on M_b. If, for safety reasons, the lowest possible value of N in Table 1 is used (i.e., pinned connection assumed at A, see Fig. 5(b)), the value of $N_{(B)} = M_b{\cdot}1318.1$ kN/4402 kN·m for scenario (B) and $N_{(C)} = M_b{\cdot}1629.4$ kN/4402 kN·m for scenario (C). The table shows that the bending moment resistance $M_{F,R}$ predicted by the component method lies between $M_{F,R,(B)}$ = 5836.4 kN·m and $M_{F,R,(C)}$ = 5909.3 kN·m, depending on the boundary conditions at point A. This results in a maximum applied force between $F_{E,R,(B)}$ = 3028.8 kN and

Table 5
Component and moment resistance for joint C2.

Bolt row, r	1	2	3	4	5	6	7	8
Lever arm, z, mm	954	834	714	594	474	354	234	114
Scenario (A) Analysis without force R_H								
Force in bolt row limited by:								
[CWT] Column web in tension, kN	3399	2529	2741	2017	2356	3024	3399	3399
[CFB] Column flange in bending, kN	2332	1013	2302	2332	2332	2332	2332	2332
[BT] Bolts in tension, kN	2746	2746	2746	2746	2746	2746	2746	2746
[EPB] End plate in bending, kN	2302	1722	1949	886	886	1214	2100	2302
[BWT] Beam web in tension, kN	4829	3753	3965	3240	3579	4247	4586	4586
Mínimum of all tension components	2302	1013	1949	886	886	1214	2100	2302
[BWC] Beam web/flange compr., kN				10158				
[CWC] Column web compr., kN				9059				
[CWS] Column web in shear, kN				6707				
Mínimum of all components	2302	1013	1949	886	557	0	0	0
Bolt row bending moment, kN·m	2196	845	1392	526	264	0	0	0
Moment resistance, $M_{R,F}$, kN·m				5222.8				
Scenario (B) Analysis with force R_H[a], assuming the column base as pinned								
[CWS] Column web in shear, kN				8538				
Mínimum of all components	2302	1013	1949	886	886	886	617	0
Bolt row bending moment, kN·m	2196	845	1392	526	420	314	144	0
Moment resistance, $M_{R,F}$, kN·m				5836.4				
Scenario (C) Analysis with force R_H[a], assuming the column base as fixed								
[CWS] Column web in shear, kN				8895				
Mínimum of all components	2302	1013	1949	886	886	886	886	87
Bolt row bending moment, kN·m	2196	845	1392	526	420	314	207	10
Moment resistance, $M_{R,F}$, kN·m				5909.3				

[a] *Components other than [CWS] for scenarios (B) and (C) are the same as in (A).*

$F_{E,R,(C)}$ = 3066.6 kN, slightly below (95.9% and 97.1%, respectively) the maximum experimental force on the test ($F_{E,max}$ = 3158.9 kN). Notice that these values are based on the as-measured yield strength of the plates and do not include any strain hardening effects, which are naturally present on the test. Neglecting force N results in a too conservative value ($M_{F,R,(A)}$ = 5222.8 kN·m, $F_{E,R,(A)}$ = 2710.3 kN). The assumed reactions (see Fig. 5) are $N_{(B)}$ = 1831.1 kN for scenario (B) and $N_{(C)}$ = 2187.3 kN for scenario (C), and are equal to the column shear force V_c, see Fig. 24(a); this internal force opposes the bolt forces and has a beneficial effect on the web panel resistance that must be properly considered, as discussed below. The critical components in the tension zone for scenarios (B) or (C) are: for row 1, EPB; for row 2, CFB; for rows 3 to 8, EPB. Globally, the column web panel in shear (CWS) is the critical component, i.e., the component whose resistance limits the overall joint resistance. It is worth noting that, for the first bolt row, the resistance of the column flange in bending (CFB) and end plate in bending (EPB) is very similar; if the assumed yield line in Fig. 25 is moved at 0.8 $\cdot l_w$, the end plate resistance increases and the column flange in bending becomes the critical component. The predictions of the component method correspond well to the observed deformations of the specimen, see Fig. 13 and Fig. 26, except that EN 1993-1-8 precludes bolt stripping failure. The column web panel is not slender (d_c/t_{wc} = 44 < 69 $\cdot\varepsilon$, where d_c is the column free web height, t_{wc} the column web thickness, and ε is (235 MPa/f_y)$^{0.5}$) therefore, no shear instability modes are expected in the web, and a ductile behaviour is predicted by the component method and confirmed by the considerable quasi-horizontal plateau in the post-peak moment–rotation curve.

The initial stiffness of the joint and the components contributing to the beam–column connection deformability, normalized by the Young Modulus E, are listed in Table 6. A particular feature of this joint is the reduced stiffness of the web column in tension, which is an order of magnitude below all other components and dominates the bolt row stiffness. This is due to the large column height. The equivalent connection lever arm is z_{eq} = 710 mm, and the equivalent stiffness k_{eq} = 10.5 mm, corresponding to an initial rotational stiffness $S_{conn,ini}$ = 1108 kN·m/mrad. Following EN 1993-1-8, the effective stiffness of the compression zone is assumed as infinite due to the presence of a strong stiffener. The web panel stiffness is k_{wp} = 14.3 mm, whereupon the joint initial rotational stiffness is $S_{j,ini}$ = 639 kN·m/mrad. The secant stiffness at M_R is $S_{j,sec}$ = 214 kN·m/mrad. For preloaded bolts, an infinite initial stiffness should be considered [41]; the bolt flexibility can be removed from the equivalent stiffness, which increases the connection stiffness to 1256 kN·m/mrad, and the joint stiffness to 688 kN·m/mrad. The stiffness reduces as the load is applied and bolt decompression gradually occurs, therefore the secant stiffness is unaffected by this phenomenon.

5. Analysis of results

5.1. Overall joint performance

Fig. 27(a) compares the moment–rotation curves obtained for the test, FEM_NoSH, and FEM_CAL. An additional curve, 'Test-NoStripping' has been added, showing a reconstituted test curve in which the post-stripping portion of the test moment–rotation curve is attached to the point where bolt-stripping is initiated. An excellent agreement is shown between the curves. Fig. 27(b) shows a comparison between the FEM_NoSH moment–rotation curve and the bilinear curve predicted by EN-1993-1-8 (curve EC3), including the limits for classification of the joint as per EN 1993-1-8, assuming a value of 20 m for the beam span (see Fig. 1), whereupon to be classified as 'rigid' the joint should present a stiffness of 955 kN·m/mrad (braced system) or 2983 kN·m/mrad (unbraced system), and to be classified as 'pinned' the stiffness should be smaller than 60 kN·m/mrad. The joint tangent stiffness at the origin according to EC3 is $S_{j,ini,EC3}$ = 639 kN·m/mrad, qualifying as 'semi-rigid' According to FEM_NoSH, $S_{j,ini,FEM}$ = 737 kN·m/mrad (calculated at 0.67$M_{R,F}$). The secant stiffness at $M_{F,R}$ according to EC3 is $S_{j,sec,EC3}$ = 214 kN·m/mrad, and according to FEM_NoSH is $S_{j,sec,FEM}$ = 207 kN·m/mrad, showing very good agreement. Table 6 shows a comparison of relevant global variables between Test_NoStripping, FEM_CAL, FEM_NoSH, CM scenario (B) (pinned column base) and CM scenario (C) (fixed column base). Based on these values it is concluded that the behaviour of the structural system corresponds more closely to scenario (B) (pinned column base). The values of $M_{F,R}$ for Test_NoStripping and FEM_CAL have been obtained at $\phi_{F,R}$ = 28.6 mrad, corresponding to the peak value from

(a) (b)

Fig. 26. Joint C2 at end of test: (a) general view of the connection; (b) detail of bolt rows 1 to 3.

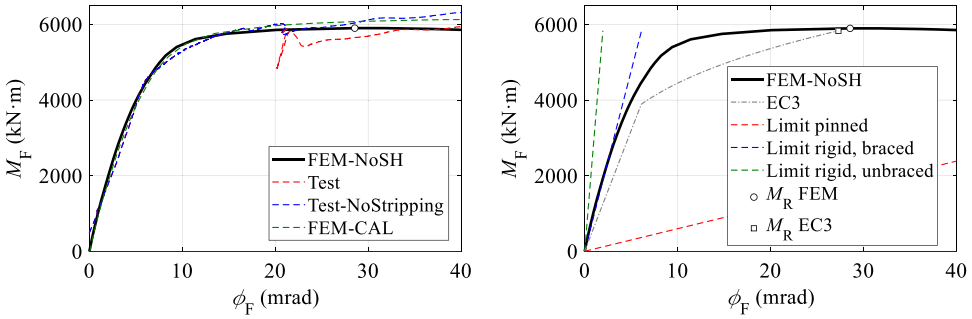

Fig. 27. Moment–rotation curve and stiffness classification of the joint.

Table 6
Normalized connection stiffness components for joint C2.

Stiffness k_r for bolt row r =	1	2	3	4	5	6	7	8
Lever arm, z, mm	954	834	714	594	474	354	234	114
[CWT] Column web in tension, mm	3.8	1.9	1.9	1.9	1.9	1.9	1.9	3.8
[CFB] Column flange in bending, mm	91.5	46.4	46.4	46.4	46.4	46.4	46.4	91.5
[BT] Bolts in tension, mm	17.3	17.3	17.3	17.3	17.3	17.3	17.3	17.3
[EPB] End plate in bending, mm	26.1	10.1	10.1	10.1	10.1	10.1	10.1	26.1
Effective bolt row stiffness $k_{eff,r}$, mm	2.68	1.43	1.43	1.43	1.43	1.43	1.43	2.68
Eff. tension zone stiffness, mm					10.5			
Eff. compression zone stiffness, mm					∞			
[CWS] column web in shear, mm					14.3			

Table 7
Comparison of global variables between FEM_NoSH and CM.

		Test_NoStripping	FEM_CAL	FEM_NoSH	CM(B)	CM(C)
$M_{F,R}$	kN·m	5992[a]	6076[a]	5900	5836	5909
$\phi_{F,R}$	mrad	28.6	28.6	28.6	27.3	27.6
$S_{j,ini}$	kN·m/mrad	645	635	737	639	639
$S_{j,sec}$	kN·m/mrad	210	213	207	219	219

[a] *Obtained for* $\phi_{F,R} = 28.6$ mrad.

FEM_NoSH. The values of secant stiffness have been obtained at this point, and the values of initial stiffness have been obtained at $0.67\,M_{F,R}$. The agreement between test, FEM and CM is excellent (see Table 7).

As discussed, according to the CM and based on the critical component (column web in shear with no buckling), this joint is classified as 'ductile'. This is also the case for the test, for which the maximum rotation reached was about 70 mrad, without a remarkable loss in resistance, as shown by Fig. 10.

5.2. Component performance

Bolt row forces are key values in the CM. They do not correspond to the addition of bolt forces in a row, because of prying forces which are difficult to measure experimentally. A properly validated FEM provides an excellent alternative to obtain their approximate values. The process followed hereby was described in Section 3.4. The resulting bolt row forces for bending moment $M_{F,R} = 5900$ kN·m are listed in Table 8, alongside with the bolt row forces predicted in the component model

Table 8
Bolt row forces from FEM and CM.

	Bolt row r						
	1	2	3	4	5	6	7
Bolt force $F_{BT,r}$, FEM (kN)	2318	2597	2481	2380	2126	1822	1806
Prying force, $F_{pry,r}$, FEM (kN)	162	702	1167	1069	1068	1254	1711
Bolt row force, F_r, FEM (kN)	2157	1895	1315	1311	1058	567	95
Bolt row force, F_r, CM (kN)	2302	1716	1218	886	886	886	669

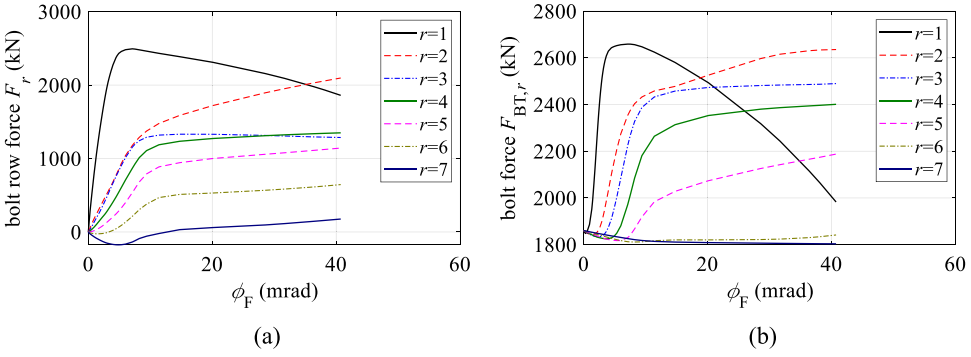

Fig. 28. Bolt row forces and bolt forces vs. joint rotation: (a) bolt row forces; (b) bolt forces.

(CM). Bolt row 8 is not displayed because it displays compression in the FEM_NoSH. The evolution of the bolt row forces and bolt forces with the joint rotation is shown in Fig. 28.

The joint shows a considerable capacity of redistribution. After bolt row one fails by thread stripping, the second bolt row force increases, see Fig. 28(a); in the test, following an initial slip, the first bolt row displacement was stopped by the nut locking on the deformed threads, resulting on a residual bolt capacity, albeit one that could not be measured experimentally. Incidentally, the FEM model is partly capable of mimicking this phenomenon, due to two features: (i) total yielding of the bolt shanks on the first bolt row, whose deformation is then controlled by the adjacent bolts; (ii) additional bending moments in the bolt shank (due to large rotation of both column flange and end plate) resulting in reduced axial force resistance of the bolt. FEM results immediately before the point where thread stripping occurs in the test, show a remarkable decrease in the bolt force, even if the overall joint resistance increases. The large curvature of the bolt shank observed both in the test and the FEM might be an indication that thread stripping is triggered by the large bending moment in the bolt due to the considerable rotation of the gripped plates. Further study is needed to determine if this is a consequence of the joint size, or it can be considered a general phenomenon.

The component deformation observed in the test and the FEM_NoSH is consistent with the predictions obtained with the CM. The CM identifies the CWS as the critical component in bolt row 7, and this is corroborated by the FEM, see Fig. 22(a). The CM identifies a unique critical component in each bolt row, but in the FEM several components present yielding at the same time, with varying degrees.

The largest difference in behaviour is on the CWT component, which in the FEM is largely yielded, even if the bolt row forces are well below the individual resistance predicted by the CM. The reason is that these resistances are obtained from the web of a notional T-stub, with an individual value and a group value, leading to notional lengths well above the actual spacing between bolt rows. In the FEM, the group effects seem to be small, and the yield pattern for internal bolt rows corresponds to individual T-stubs with no interaction between them, leading to a larger concentration of the bolt row force in the CWT for internal bolt rows than predicted. Correspondingly, at least for the CWT and BWT components, the individual notional length of the T-stub corresponding to an internal bolt row should not exceed the spacing between bolt rows.

The individual component stiffness can be obtained from the FEM dividing the bolt row force over the component deformation. For consistency with the CM, this is done at $0.67 \cdot M_{F,R}$. The results are shown in Table 9. In this table, the bolt stiffness only makes sense when the bolt force is above the preload value, as indicated by the column labelled as $F_{BT,r} - F_{p,C}$. By comparison with Table 6, individual differences exist. The most remarkable is on the CWT stiffness, which is clearly underestimated by the component method. Overall, the effective stiffness obtained from the FEM is clearly above the one obtained from the CM. This is also shown by the differences on the joint stiffness listed in Table 6; however, these differences are somewhat softened by the influence of the CWS.

6. Summary and conclusions

An experimental test on a large-scale beam–column joint has been performed. The results of the test indicate that:

- The joint showed an adequate level of resistance, failing at 2.1 times the design target.
- The joint showed a large deformation capacity, featuring a maximum rotation of 70 mrad (limited by the experimental setup) with no apparent loss of resistance, except for one sudden slip attributed to thread stripping of the bolts in the first bolt row.
- The joint resistance increased steadily after thread stripping, showing a remarkable resilience and redistribution capacity.
- Thread stripping happened even though the HR bolts used are intended to fail by plastic deformation of the bolt shank. Thread stripping seems to be precipitated by the conspicuous curvature of the bolt shank in the first bolt row, due to the relative rotation between end plate and column flange and might be a specific feature of large joints. Additional research is needed to address this specific phenomenon.

To further understand the behaviour of the joint, high-quality FE models and manual calculations according to the component method have

Table 9
Individual component stiffness calculated from FEM.

r	F_r (kN)	$F_{BT,r}$ (kN)	$F_{BT,r} - F_{p,C}$ (kN)	$k_{EPB,r}$ (mm)	$k_{BT,r}$ (mm)	$k_{CFB,r}$ (mm)	$k_{CWT,r}$ (mm)	$k_{eff,r}$ (mm)
1	2458.3	2652.3	792.3	13.7	15.1	23.6	17.0	4.2
2	934.1	2206.8	346.8	6.6	84.5	12.7	5.4	2.4
3	904.9	2002.5	142.5	11.5	221.9	27.2	6.0	3.4
4	606.3	1848.7	−11.3	15.6		43.4	5.4	3.7[a]
5	327.4	1817.3	−42.7	20.5		110.4	4.9	3.8[a]
6	89.8	1821.2	−38.8	28.3		−30.7	6.8	6.6[a]

[a]*Excluding the bolt row stiffness.*

also been presented. A novel and simple methodology for the exploitation of the FEM results has been presented, allowing for the extraction of detailed component results that provide a deep understanding of the individual joint components. The results show that:

- The FEM and CM reproduce well the behaviour of the joint and lead to reasonable predictions of the joint overall resistance and stiffness.
- The FEM and CM give reasonably similar results of the bolt row forces.
- The individual stiffness of the components seems to be underestimated in the CM when compared to the FEM.

The following relevant issues are identified in relation with the component 'bolt in tension' (BT).

- The limit $\varepsilon_{pl,lim} = 2.3\%$ set in prEN 1993-1-14 seems to be very restrictive, leading to theoretical values well below the maximum resistance observed in the tests.
- EN 1993-1-8 characterizes this component only for tension. However, compatibility with the gripped plates results in shank curvature and therefore bending. The combined bending and tension produce larger stress and strain and may be the cause of the thread stripping observed in the tests. Although an interaction equation can be used to approximate this behaviour, there is a lack of experimental evidence on the validity of such an approach.

Finally, it can be concluded that a properly designed (following the EN 1993-1-8 recommendations) bolted beam-to-column joint connecting very large profiles achieves its plastic moment resistance, behaves in a ductile way and the component method gives reliable predictions of its mechanical properties.

CRediT authorship contribution statement

L. Simões da Silva: Writing – review & editing, Writing – original draft, Methodology, Investigation, Funding acquisition, Conceptualization. **Hélder Craveiro:** Writing – review & editing, Writing – original draft. **Jorge Conde:** Writing – review & editing, Writing – original draft, Investigation, Conceptualization. **Rui Simões:** Writing – review & editing. **Claúdio Martins:** Writing – review & editing. **Andrea Catinaccio:** Writing – review & editing. **Dimitar Mladenov:** Writing – review & editing. **João Batista Lopes:** Writing – review & editing. **Diego Alvarez Feito:** Writing – review & editing. **Christophe Bault:** Writing – review & editing.

Declaration of competing interest

I declare on behalf of myself and all the authors that there is no conflict of interest.

Data availability

Data will be made available on request

Acknowledgment and funding sources

This work was partly financed by:

- FCT/MCTES through national funds (PIDDAC) under the R&D Unit Institute for Sustainability and Innovation in Structural Engineering (ISISE), under reference UIDB/04029/2020, and under the Associate Laboratory Advanced Production and Intelligent Systems (ARISE) under reference LA/P/0112/2020.
- Grant with reference UP2021-035 (RD 289/2021) from "Ministerio de Universidades de España", funded by European Union, NextGenerationEU, attributed to Jorge Conde.

Annex A. Mechanical properties of steel

See Tables A.1–A.4.

Annex B. Supplementary data

Supplementary material related to this article can be found online at https://doi.org/10.1016/j.tws.2023.110996.

Table A.1
Measured and calculated values for the coupon specimens extracted from the web, longitudinal (L) and transverse (T) to rolling.

Sample	Measured				Calculated			
	$F_{p,0.2\%}$ [N]	F_m [N]	L_u [mm]	E [GPa]	$R_{p,0.2\%}$ [N/mm^2]	R_m [N/mm^2]	A [%]	ε_u [%]
Web, parallel to rolling direction								
Web_{L1}	210460	263396	151.2	194.5	470	588	26	10.11
Web_{L2}	207376	266198	152.5	208.9	463	594	27.1	10.71
Web_{L3}	205743	267566	151.7	196.5	461	600	26.4	10.66
Mean	207860	265720	151.8	199.9	464.7	594.0	26.5	10.49
CoV	1.15%	0.80%	0.43%	3.9%	1.02%	1.01%	2.10%	3.19
Web, perpendicular to rolling direction								
Web_{T1}	208558	273822	147.3	211.2	467	614	22.8	9.51
Web_{T2}	210623	273968	148.2	210.4	472	614	23.5	9.87
Web_{T3}	210853	273517	147.5	210.4	473	613	22.9	9.94
Mean	210011	273769	147.7	210.6	470.7	613.7	23.2	9.77
CoV	0.60%	0.08%	0.32%	0.22%	0.68%	0.09%	2.14%	2.34%

Table A.2
Measured and calculated values for the coupon specimens extracted from the flange, longitudinal (L) and transverse (T) to rolling.

Sample	Measured				Calculated			
	$F_{p,0.2\%}$ [N]	F_m [N]	L_u [mm]	E [GPa]	$R_{p,0.2\%}$ [N/mm^2]	R_m [N/mm^2]	A [%]	ε_u [%]
Flange, parallel to rolling direction								
$Flange_{L1}$	243717	297472	155.9	176.8	491	599	24.7	11.26
$Flange_{L2}$	245690	298743	156	–	493	599	24.8	11.25
$Flange_{L3}$	253423	308629	155.6	213.9	506	617	24.5	10.23
Mean	247610	301615	155.8	195.4	496.7	605.0	24.7	10.91
CoV	2.07%	2.03%	0.13%	13.4%	1.64%	1.72%	0.62%	5.44%
Flange, perpendicular to rolling direction								
$Flange_{T1}$	228532	284753	159.6	196.3	474	590	27.7	11.34
$Flange_{T2}$	223604	285153	156.8	187.8	462	589	25.4	12.76
$Flange_{T3}$	220717	285329	155.3	199.4	456	589	24.2	11.38
Mean	224284	285078	157.2	194.5	464.0	589.3	25.8	11.83
CoV	1.76%	0.10%	1.39%	3.09%	1.98%	0.10%	6.90%	6.84%

Table A.3
Measured and calculated values for the coupon specimens extracted from the end plate, longitudinal (L) and transverse (T) to rolling.

Sample	Measured				Calculated			
	$F_{p,0.2\%}$ [N]	F_m [N]	L_u [mm]	E [GPa]	$R_{p,0.2\%}$ [N/mm^2]	R_m [N/mm^2]	A [%]	ε_u [%]
$End\text{-}plate_1$	259493	296115	155	198.6	516	589	24	8.15
$End\text{-}plate_2$	259114	296114	155.9	181.7	516	589	24.7	8.14
$End\text{-}plate_3$	260393	297936	155.5	200.8	518	593	24.4	8.24
Mean	259666.7	296721.7	155.5	193.7	516.7	590.3	24.4	8.18
CoV	0.25%	0.35%	0.29%	5.4%	0.22%	0.39%	1.44%	0.67%

Table A.4
Measured and calculated values for the round coupon specimens extracted from M48 bolts (HV and HR).

Sample	Measured				Calculated			
	$F_{p,0.2\%}$ [N]	F_m [N]	L_u [mm]	E [GPa]	$R_{p,0.2\%}$ [N/mm^2]	R_m [N/mm^2]	A [%]	ε_u [%]
HR bolts								
$(HR\text{-}M48\text{-}10.9)_1$	290131	326010	112	210.0	924	1039	12	5.07
$(HR\text{-}M48\text{-}10.9)_2$	286297	323252	114.1	204.7	908	1025	14.1	5.84
$(HR\text{-}M48\text{-}10.9)_3$	292743	328099	112.7	213.4	931	1043	12.7	5.16
Mean	289724	325787	112.9	209.4	921.0	1035.7	12.9	5.35
CoV	1.12%	0.75%	0.95%	2.09%	1.28%	0.91%	8.3%	7.82%
HV bolts								
$(HV–M48–10.9)_1$	323490	351920	114	197.9	1038	1129	14	3.45
$(HV–M48–10.9)_2$	347259	374677	115.2	201.2	1098	1184	15.2	3.73
$(HV–M48–10.9)_3$	327939	356795	113.9	200.4	1044	1136	13.9	3.64
Mean	332896	361131	114.4	199.8	1060.0	1149.7	14.4	3.61
CoV	3.80%	3.32%	0.63%	0.86%	3.12%	2.60%	5.0%	3.91%

References

[1] FERMILAB, Fermi National Accelerator Laboratory, Facility for the Deep Underground Neutrino Experiment, FERMILAB, 2019, viewed 1 2019, < https://lbnf.fnal.gov/>.

[2] L. Simões da Silva, Towards a consistent design approach for steel joints under generalized loading, J. Construct. Steel Res. 64 (9) (2008) 1059–1075.

[3] C. Faella, V. Piluso, G. Rizzano, Structural Steel Semirigid Connections: Theory, Design and Software, CRC Press LLC, USA, 2000.

[4] J.P. Jaspart, K. Weynand, Design of Joints in Steel and Composite Structures, ECCS Press and Ernst & Sohn, Brussels, Belgium, 2016.

[5] P. Zoetemeijer, A design method for the tension side of statically loaded, bolted beam-to-column connections, Heron 20 (1) (1974) 1–59.

[6] H. Aggerskov, Analysis of bolted connections subjected to prying, J. Struct. Div. ASCE 103 (ST11) (1977) 2145–2163.

[7] V. Piluso, C. Faella, G. Rizzano, Ultimate behavior of bolted T-stubs. I: Theoretical model, J. Struct. Eng. ASCE 127 (6) (2001) 686–693.

[8] H. Krawinkler, V. Bertero, E.G. Popov, Shear behaviour of steel frame joints, J. Struct. Div. ASCE 101 (ST11) (1975) Nov. 1975.

[9] J.P. Jaspart, Etude de la semi-rigidité des nøeuds poutre-colonne et son influence sur la résistance et la stabilité des ossatures en acier (Ph.D. Thèse), Faculté des Sciences Appliquées, Université de Liège, 1991.

[10] J.M. Aribert, A. Lachal, M. Moheissen, Interaction between local buckling and strength of a hot-rolled profile under to local double compression (steel grades up to FeE 460) (in French), Constr. Métall. (2) (1990) 3–23.

[11] EN 1993-1-8, Eurocode 3: Design of Steel Structures – Part 1-8: Design of Joints, European Committee for Standardization, Brussels, Belgium, 2005.

[12] ANSI/AISC 360-16, Specification for Structural Steel Buildings, American Institute of Steel Construction, Chicago, USA, 2016.

[13] P.J.S. Cruz, L. Simões da Silva, D.S. Rodrigues, R.A.D. Simões, Database for the semi-rigid behaviour of beam-to-column connections in seismic regions, J. Construct. Steel Res. 46 (1–3) (1998) 120.

[14] K. Weynand, M. Huter, P. Kirby, L. Simões da Silva, P. Cruz, Sericon – a databank for tests on semi-rigid joints, in: Proceedings of the COST C1 International Conference on Control of the Semi-Rigid Behaviour of Civil Engineering Structural Connections, Liège, Belgium, 1998, pp. 217–228.

[15] P. Nogueiro, L. Simões da Silva, R. Bento, R. Simões, Numerical implementation and calibration of a hysteretic model with pinching for the cyclic response of steel joints, Adv. Steel Constr. 3 (1) (2007) 128–153.

[16] T. Sullivan, G. O'Reilly (Eds.), Characterizing the Seismic Behaviour of Steel Beam-To-Column Joints for Seismic Design, IUSS Press, Eucentre, Italy, 2014.

[17] SEI, Multiple Row Extended End-Plate Connection Tests, Research report Structural Engineers. Inc., Norman, OK, 1984.

[18] S. Morrison, A. Astaneh-Asl, T. Murray, Analytical and Experimental Investigation of the Multiple Row Extended Moment End-Plate Connection with Eight Bolts at the Beam Tension Flange, Research Report FSEL/MBMA 84-04, Fears Structural Engineering Laboratory. University of Oklahoma, Norman, OK, 1986.

[19] J. Borgsmiller, E. Summer, T. Murray, Tests of Extended Moment End-Plate Connections Having Large Inner Pitch Distances, Research Report CE/VPI-ST-95/01, Department of Civil Engineering. Virginia Polytechnic Institute and State University, Blacksburg VA, 1995.

[20] J. Ryan, Evaluation of Extended End-Plate Moment Connections Under Seismic Loading (Master of Science Civil Engineering Thesis), Virginia Polytechnic Institute, 1999.

[21] E. Summer, Unified Design of Extended End-Plate Moment Connections Subject to Cyclic Loading (Dissertation), Submitted to the Faculty of the Virginia Polytechnic Institute, 2003.
[22] L. Katula, L. Dunai, Full scale tests on bolted beam-to-beam end-plate connections under bending, Bauingenieur Band 84 (2009) 132–138.
[23] M.R. Bahaari, A.N. Sherbourne, Behavior of eight-bolt large capacity endplate connections, Comput. Struct. 77 (3) (2000) 315–325.
[24] P. Kawecki, J. Laguna, A. Kozlowski, Fem analysis of the extended end-plate splice of welded i-girders with multiple bolt rows and bolts per row, in: Gizejowski, et al. (Eds.), Recent Progress in Steel and Composite Structures, Taylor & Francis Group, London, ISBN: 978-1-138-02946-0, 2016, pp. 443–450.
[25] FprEN 1993-1-1, Eurocode 3: Design of Steel Structures – Part 1-1: General Rules and Rules for Buildings, European Committee for Standardization, Brussels, Belgium, 2022.
[26] ISO 6892-1:2009, Metallic Materials - Tensile Testing - Part 1: Method of Test at Room Temperature, International Organization for Standardization, Geneva, 2009.
[27] EN 10025-4:2004, Hot Rolled Products of Structural Steels. Part 4: Technical Delivery Conditions for Thermomechanical Rolled Weldable Fine Grain Structural Steels, European Committee for Standardization, Brussels, Belgium, 2004.
[28] ISO 898–1, Mechanical Properties of Fasteners Made of Carbon Steel and Alloy Steel, International Organization for Standardization, Switzerland, 2009.
[29] Simulia, Abaqus User Manual, Dassault systems Simulia Corp., 2021, [online]. Last accessed 06/01/2023. Available at: https://help.3ds.com/HelpProductsDS.aspx.
[30] P. Arasaratnam, K.S. Sivakumaran, M.J. Tait, True stress-true strain models for structural steel elements, Int. Sch. Res. Not. 2011 (2011).
[31] O. Bursi, J.P. Jaspart, Benchmarks for finite element modelling of bolted steel connections, J. Construct. Steel Res. 43 (1–3) (1997) 17–42.
[32] prEN 1993-1-14, Eurocode 3: Design of Steel Structures – Part 1-14: Design Assisted by Finite Element Analysis, European Committee for Standardization, Brussels, Belgium, 2022.
[33] L. Simões da Silva, L. Lima, P. Vellasco, S. Andrade, Behaviour of flush end-plate beam-to-column joints subjected to bending and axial force, Steel Compos. Struct. 4 (2) (2004) 77–94.
[34] J.M. Castro, A.Y. Elghazouli, B.A. Izzuddin, Modelling of the panel zone in steel and composite moment frames, Eng. Struct. 27 (2005) 129–144.
[35] S. Jordão, L. Simões da Silva, R. Simões, Behaviour of welded beam-to-column joints with beams of unequal depth, J. Construct. Steel Res. 91 (2013) 42–59, 2013.
[36] K. Weynand, J.P. Jaspart, M. Steenhuis, The stiffness model of revised annex j of eurocode 3, in: R. Bjorhovde, A. Colson, R. Zandonini (Eds.), Connections in Steel Structures III. Proceedings of the 3rd International Workshop on Connections, 1995, pp. 441–452.
[37] L. Simões da Silva, A. Santiago, P. Vila Real, A component model for the behaviour of steel joints at elevated temperatures, J. Constr. Steel Res. 57 (11) (2001) 1169–1195.
[38] S. Oliveira, R. Costa, A. Shabazian, C. Rebelo, Y. Harada, L. Simões da Silva, A component-based model for the cyclic behaviour of steel joints, J. Construct. Steel Res. 181 (2021) 106551, 2021.
[39] L. Simões da Silva, S. Oliveira, R. Costa, F. Gentili, Design and analysis of steel structures considering the 3D behaviour of the joints, Adv. Steel Constr. 16 (2) (2020) 137–145.
[40] T. Golea, A. Corman, J. Mathieu, Y. Duchêne, J.P. Jaspart, J.F. Demonceau, An innovative mechanical model for structural steel joints, Eng. Struct. 277 (2023) 115459.
[41] FprEN 1993-1-8, Eurocode 3: Design of Steel Structures – Part 1-8: Joints, European Committee for Standardization, Brussels, Belgium, 2022.